LA-UR-90-1360

LA-UR--90-1360

DE90 010603

CONF-8908131--6

MAY 0 9 1990

Los Alamos National Laboratory is operated by the University of California for the United States Department of Energy under contract W-7405-ENG-36

TITLE CORRELATIONS, NUCLEAR STRUCTURE, AND DCX

AUTHOR(S) W. B. Kaufmann and W. R. Gibbs

SUBMITTED TO "Proceedings at The Second LAMPF International Workshop on Pion-Nucleus Double Charge Exchange" (World Scientific), Los Alamos, NM, August 1989

DISCLAIMER

This report was prepared as an account of work sponsored by an agency of the United States Government. Neither the United States Government nor any agency thereof, nor any of their employees, makes any warranty, express or implied, or assumes any legal liability or responsibility for the accuracy, completeness, or usefulness of any information, apparatus, product, or process disclosed, or represents that its use would not infringe privately owned rights. Reference herein to any specific commercial product, process, or service by trade name, trademark, manufacturer, or otherwise does not necessarily constitute or imply its endorsement, recommendation, or favoring by the United States Government or any agency thereof. The views and opinions of authors expressed herein do not necessarily state or reflect those of the United States Government or any agency thereof.

By acceptance of this article, the publisher recognizes that the U.S. Government retains a nonexclusive, royalty-free license to publish or reproduce the published form of this contribution, or to allow others to do so, for U.S. Government purposes.

The Los Alamos National Laboratory requests that the publisher identify this article as work performed under the auspices of the U.S. Department of Energy

MASTER

Los Alamos National Laboratory
Los Alamos, New Mexico 87545

FORM NO 836 R4

Correlations, Nuclear Structure, and DCX

W. B. Kaufmann and W. R. Gibbs

Theoretical Division
Los Alamos National Laboratory
Los Alamos, NM 87545

and

Department of Physics
Arizona State University
Tempe, AZ 85287

Aug. 9, 1989

Abstract

To what extent can we understand current low-energy DCX cross sections to the DIAS in terms of the sequential mechanism? What do the results have to say about the nuclear wave functions?

1 CORRELATIONS

One of the principal goals of the pion double charge exchange (DCX) program is to learn about the relative placement of nucleons in the nucleus: the correlations. We will focus on this aspect of DCX.

We recall one plausible conclusion from our contribution to the first DCX Workshop [1-2] : DCX occurs mainly when the active nucleons, i.e. those which exchange charge with the pion, are close to one another (within about 1.5 fm.). Thus examine the short-range structure of the nuclear wave functions that we plan to use in our calculations.

As a tool to get an intuitive picture of the correlation structure we will fix one of the nucleons at r_1 and evaluate the probability $P_\epsilon(r_1)$ that the second nucleon is within a distance ϵ of it. This is a simple 2-fold integral (the axial integration is trivial) however complicated the two-body wave function. The probability could then be evaluated for various positions of the first nucleon and for different values of ϵ.

There are many other ways of representing the nucleon-nucleon correlations. The separation density of Bleszynski and Glauber [3] is one, the standard two-body correlation function discussed by Zamick [4] is another. The Monte-Carlo plots we have given in [2] showing the contribution to the amplitude corresponding to different nucleon-nucleon separations is still another. The present representation is very simple, and it fits very well with the correlation analysis presented in Section 3.

1.1 ^{14}C Configuration Map, p-shell Model

We begin with a simple system with two valence particles in the 1p-shell, which is a simple model of ^{14}C as two proton holes in a filled p-shell. There are two independent basis vectors for a 0^+ state, which we choose as $1p_{\frac{3}{2}}$ and $1p_{\frac{1}{2}}$. Since the two configurations have similar energies, the ground state is better represented by a normalized linear combination of the two, viz.,

$$|\Psi>=cos(m)|(1p_{\frac{3}{2}})^2> +sin(m)|(1p_{\frac{1}{2}})^2> \qquad (1)$$

where m is a mixing angle. To decide the value of m which best approximates the physical ground state must introduce additional physics, such as the diagonalization of a model residual hamiltonian.

If the radial portions of the $1p_{\frac{3}{2}}$ and $1p_{\frac{1}{2}}$ wave functions are identical then the radial dependence factors out of the sum. In this case the correlations depend only on the angle between the vectors from the center of the nucleus to each of the nucleons. There are no radial correlations, in the sense that the mixture between $1p_{\frac{1}{2}}$ and $1p_{\frac{3}{2}}$ wave functions is independent of the distance either particle is found from the origin.

Fig. 1 displays $P_{t=1}(r_1 = 2)$ *vs.* the mixing angle, m. The first nucleon is fixed at a distance $r_1 = 2$ fm from the origin; the second nucleon lies within 1 fm of the first nucleon. A very strong dependence on the mixing angle is evident. 0° represents pure $(1p_{\frac{3}{2}})^2$ while 90° corresponds to pure $(1p_{\frac{1}{2}})^2$. As is easily seen from coupling the spherical harmonics of the single-particle wave functions with Clebsch-Gordan coefficients, the $(1p_{\frac{1}{2}})^2$ state has no angular correlations, i.e. knowledge of the direction of the vector $\vec{r}_1$ describing the position of the first particle gives no information about $\vec{r}_2$, the direction of the second. All other values of the mixing angle correspond to definite correlations. For example, if $cos(m) = \sqrt{\frac{2}{3}}$ (i.e. m approximately 35°) the the wave function has L=S=0, for which the density is proportional to $3(\vec{r}_1 \cdot \vec{r}_2)^2$. This configuration optimizes close correlation of the neutron pair; the spatial portion of the wave function is totally symmetric. Near 125° the there is much less chance of finding the particle in the 1 fm sphere than would be found with uncorrelated wave functions; this is the case L=S=1 in which the spatial portion of the wave function is antisymmetric.

Because in this example the $1p_{\frac{1}{2}}$ and $1p_{\frac{3}{2}}$ radial functions are the same, the general shape of the curve is independent of the specific value of $\vec{r}_1$. A physical solution of Cohen and Kurath [5] is also plotted on the curve. The correlation probability lies intermediate between the pure $1p_{\frac{1}{2}}$ configuration and the maximally correlated L=S=0 combination.

If (by virtue of a spin-orbit potential, for example) the radial functions are not identical the relative amounts of the $1p_{\frac{3}{2}}$ and $1p_{\frac{1}{2}}$ configurations change with the distance of the two particles from the origin. In this case there are radial correlations in addition to the angular ones.

1.2 ^{18}O Configuration Map, sd-Shell Model

A similar model of ^{18}O which now includes the three configurations of the sd-shell requires a more complicated plot. We assume that

$$\begin{aligned} |^{18}\mathrm{O}> &= cos(\theta)|(1d_{\frac{5}{2}})^2> \\ &\quad +sin(\theta)[cos(\phi)|(1d_{\frac{3}{2}})^2> +sin(\phi)|(2s_{\frac{1}{2}})^2>] \end{aligned} \qquad (2)$$

The configuration is represented by a point on a unit sphere determined by angles θ and ϕ. The polar angle θ $(0 < \theta < \pi)$ determines the amount of $1d_{\frac{5}{2}}$ state in ^{18}O. If $\theta = 0$ or $\theta = \pi$ the state is pure $1d_{\frac{5}{2}}$; if $\theta = \frac{\pi}{2}$ there is no $1d_{\frac{5}{2}}$ present. The azimuthal angle ϕ determines the relative amounts of the $2s_{\frac{1}{2}}$ and $1d_{\frac{3}{2}}$ states within the state vector. In principle ϕ varies between 0 and 2π, but because antipodes represent the same physical state we need only look at a hemisphere, so we will take $0 < \phi < \pi$. In our plots we use a mercator projection in which x represents the equatorial axis and y, the polar one. The z-axis will represent the quantities of interest, in fig. 2 the probability that the particles lie within 1 fm of each other.

Fig. 2 shows that as with ^{14}C in ^{18}O there is also a very strong sensitivity of the correlation probability to the relative amounts of each configuration. The deep valley cutting across the terrain define states with strong anti-correlations. The mountain ridges define positively-correlated wave functions in which the nucleons move in closer company. Fig. 3 shows the same geography in mercator projection. The line defined by $tan(\theta)cos(\phi) = \sqrt{\frac{2}{3}}$, which runs across the mountain ridge, gives spatially symmetric L=S=0 states. The points on the valley floor marked by 'o' define the pure antisymmetric L=S=1 state defined by $cos(\theta) = -\sqrt{\frac{2}{5}}$ and $\phi = 0$.

A shell model including the full sd-shell [6] gives $\theta = 33°$ and $\phi = 63°$. A shell-model calculation restricted to the $1d_{\frac{5}{2}}$ and $2s_{\frac{1}{2}}$ orbitals [7] gives $\theta = 20°$ and $\phi = 90°$. These points are marked on fig. 3. As with the Cohen-Kurath ^{14}C mixture this corresponds to neither the most or the least correlated states.

For ^{18}O the radial wave functions are certainly different (because one is an s-wave) so that the mixture varies with the distance of the nucleons from the origin. We have chosen $r_1 = 2$ fm which is a typical point at which the first charge-exchange might occur. The mixture changes rather slowly with r_1 (even though this is near the radial node in the 2s radial function): the terrain is rather similar for a large range of r_1.

1.3 ^{14}C Configuration Map, psd Shell Model

As a final example we add some sd-shell components to the model space as in the Fortune-Stephans [8] model of ^{14}C:

$$A|(1p_{\frac{3}{2}})^2> +B|(1p_{\frac{1}{2}})^2> +C|(2s_{\frac{1}{2}})^2> +D|(1d_{\frac{5}{2}})^2> . \tag{3}$$

After removing an arbitrary overall normalization factor A, B, C, and D are fixed by a 3 mixing angles such as polar coordinates for a 4-dimensional hypersphere. To determine the relative values of the constants we could diagonalize the residual interaction in a 4 x 4 space, for example. To simplify matters we, following Fortune and Stephans, use a fixed combination of the $2s_{\frac{1}{2}}$ and $1d_{\frac{5}{2}}$ configurations, viz.,

$$|sd >= 0.737|(2s_{\frac{1}{2}})^2 > +0.677|(1d_{\frac{5}{2}})^2 > \tag{4}$$

so now

$$\begin{aligned} |^{14}\mathrm{C} > \;&=\; cos(\theta)|(1p_{\frac{3}{2}})^2 > + \\ &\quad sin(\theta)[cos(\phi)|(1p_{\frac{1}{2}})^2 > +sin(\phi)|sd >]. \end{aligned} \tag{5}$$

Figs. 4 and 5 show the correlation topography of this wave function. The dominant feature is the immense 'correlation summit' near $\theta = 130°$ and $\phi = 120°$, in which the particles are extremely closely correlated. The Cohen-Kurath and Fortune-Stephans wave functions are marked. Note that the Cohen-Kurath point appears twice (on opposite sides of the unit sphere).

As the model space grows, the solution gets closer and closer to the eigenstates of the chosen residual hamiltonian, and hence it has all of the correlations implicit in the hamiltonian. The short-range complexity can be much greater than that possible in the 1p-shell.

1.4 Radial Wave Functions

DCX is sensitive to the nuclear size. This leads us to an ambiguity inherent in our choice of a small, very incomplete, basis set.

One could argue that if we wish to use the mixing angles given by shell-model calculations we should use radial wave functions consistent (at least) with the single-particle energies used in the shell-model calculations. In this article we have chosen wave function of this type, usually of harmonic-oscillator variety.

On the other hand, the simple shell-model basis functions are not likely to possess the correct single-particle separation energies or rms radii of the last neutron(s) or proton(s). The use of radial wave functions which have the correct rms radii (as measured, for example by magnetic electron scattering) would remedy this problem, but now the connection with shell-model calculations and the immense body of nuclear structure codified in them is less direct. We have also included some calculations of this type which are solutions to a Woods-Saxon potential well with the depth of the potential varied to produce the correct binding energy of the last neutron or proton.

1.5 Short-Range Correlations

If the residual interaction depended in some critical way on a short-range interaction such as rho-meson exchange between nucleons then m, and hence the wave function, could be said to depend on short-range correlations. The terms 'shell-model correlations' and 'short-range correlations' are really somewhat blurry. In some of our previous work [1-2,9] we have included 'short-range correlations' in addition to those inherent in our shell-model configurations by means of Jastrow or hard-sphere correlations, NN scattering lengths, or by a three-body model. Of these only the last is self-consistent. the others either approximate higher configurations left out by our limited basis or supply additional mechanisms omitted in the shell-model hamiltonian. These short-range correlations add structure to the nuclear wave function at a distance scale of typically a fermi. In Ref. 9. for example. we found that their main effect for low-energy DCX was to change the scale. leaving the angular distribution little changed. The effect was mainly either to lower somewhat the DCX cross sections in the case of hard-sphere correlations or to enhance them in the case of correlations with intermediate-range attraction. In the present work we adopt a minimal approach and use only the correlations present in the shell-model configurations.

2 Distorted Wave Methods

Because the pion transfers two units of charge to the nucleus the DCX operator must be a function of the coordinates of the pion and at least two nucleons. In the distorted-wave impulse approximation (DWIA) we represent the DCX operator by an effective operator of only these three coordinates; the effect of the other nuclear constituents (distortion of pion waves, excitation of the nucleus by the pion, etc.) is absorbed into this operator. If the initial and final nuclei are in a pure 0^+ state the operator may be expressed in the rather general form [9]:

$$\begin{aligned} &< \vec{k}'|F(\vec{r}_1,\vec{r}_2)|\vec{k} >= \\ &[< \vec{k}'|F_{nf}(\vec{r}_1,\vec{r}_2)|\vec{k} > + < \vec{k}'|F_f(\vec{r}_1,\vec{r}_2)|\vec{k} > (\vec{\sigma}_1 \cdot \vec{e}_1)(\vec{\sigma}_2 \cdot \vec{e}_2)]T_-(1)T_-(2). \qquad (6) \end{aligned}$$

The first term represents the spin-independent interactions and the second, the spin-dependent ones. σ_i are the spin operators of the nucleons, and e_i are model-dependent functions which depend on the particular mechanism [9]. The T's are isospin ladder operators which turn neutrons into protons. $\vec{k}$ and $\vec{k}'$ are the incident and outgoing momenta of the pion.

As in Section 1 we restrict ourselves to two nucleons (or holes) coupled to angular momentum zero outside of a closed shell, although this could be extended to allow a larger number of particles in the unfilled shells by use of shell-model density-matrix elements. Thus the nuclear wave functions may be expressed as

$$|N >= \Sigma_i C_i |(i)^2 > \qquad (7)$$

where $i = (n_i \ell_i j_i)$ describes the shell quantum numbers. The matrix elements of (1) using this nuclear wave function is

$$A = \Sigma_{ik} C_i C_k < (i)^2 | F | (k)^2 > \qquad (8)$$

This matrix element may be evaluated as [see, for example Ref. 10]

$$\begin{aligned} &< (i)^2|F|(k)^2 >= \\ &\quad \Sigma_L G^L_{ik} \int d^3r_1 d^3r_2 \; \rho_{ik}(r_1,r_2) Y_L(\vec{r}_1) \cdot Y_L(\vec{r}_2) < \vec{k}'|F(\vec{r}_1,\vec{r}_2)|\vec{k} > \\ &\quad + \text{spin-flip term} \qquad (9) \end{aligned}$$

where ρ_{ik} is the transition density, and where the factor G^L_{ik} is a combination of 3-j and 6-j symbols. For the sequential scattering process the piece of

F representing s-wave pion-nucleon charge exchange is given in coordinate space by

$$
\begin{aligned}
&< \vec{k}'|F(\vec{r}_1,\vec{r}_2)|\vec{k} >= \\
&\quad -2\,\frac{1}{2\pi^2}\int \psi_{\vec{k}'}^{(-)*}(\vec{r}_a)\; f_2^{sx}\; v(\vec{r}_a-\vec{r}_2)v(\vec{r}_2-\vec{r}_b) \\
&\quad G(\vec{r}_b,\vec{r}_c)v(\vec{r}_c-\vec{r}_1,\, v(\vec{r}_1-\vec{r}_d)\; f_1^{sx}\; \psi_{\vec{k}}^{(+)}(\vec{r}_d)\; d^3r_a d^3r_b d^3r_c d^3r_d. \qquad (10)
\end{aligned}
$$

The pion distorted waves $\psi_{\vec{k}}$ are solutions to the relativistic Lippmann-Schwinger equation with a finite-range optical potential with medium corrections [11].

$$G = (E - H_N - K_\pi - U_\pi + i\epsilon)^{-1} \qquad (11)$$

defines the Green operator [see Ref. 12] where we have approximated U_π by the same optical potential (without the Coulomb potential) used to calculate the distorted waves for the incident and outgoing charged pions. K_π is the kinetic energy of the pion. We have further approximated the nuclear hamiltonian, H_N, by a constant (closure approximation). This is probably a good approximation except at very low (less than about 30 MeV) energies. For lower energies it may be important to correct the closure approximation, perhaps through energy shifts for the different multipoles as advocated in the work of Bleszynski and Glauber [4]. The v functions represent the off-shell pion-nucleon form factors, and are taken to be of Yamaguchi form as in [11]. f^{sx} are the on-shell pion-nucleon charge-exchange amplitudes [Ref. 13 for pion energy less than 80 MeV; Ref. 14 for energies above].

The p-wave (flip and non-flip) pieces are quite similar to eqn. 10, but involve derivative operators. To perform the integral in eqn. 10 it is convenient to first define a v *transform* as a convolution of v with another function. In this language the sequential operator is the matrix product of the v-transforms of the initial pion wave function, the (double) v-transform of the Green function, and the v-transform of the final pion wave function.

3 A CONFIGURATION ANALYSIS

The most time-consuming parts of the calculation are the evaluation of the distorted waves and the Green function. The v-transforms and integrals leading to the multipoles also take considerable computer time. Once the multipoles are available, however, it is easy to vary the amplitude coefficients of each of the configurations present in the nuclear model space.

If more than two particles are present in unfilled shells, and if J=0 pairs dominate, these same multipoles may be combined with nuclear density-matrix elements to compute DCX on these more complex nuclei.

3.1 ^{14}C Configuration Analysis, p-Shell Model

We begin with the simple p-shell model of ^{14}C. Fig. 6 is a plot of the forward DCX cross section at 50 MeV as a function of the mixing angle m. There is a remarkable similarity between this and the previous correlation map for p-shell ^{14}C [see Fig.1]. This is consistent with our earlier claim that the reaction is enhanced for configurations that correspond to close nucleon pairs, at least within the reaction-theory model used. This conclusion is likely to hold up when other reaction mechanisms (DINT, MEC, and the like) are also included, because these are also very short-range mechanisms. (The weakest link here is our assumption of closure in the intermediate states. It would be interesting to examine the approach to closure through, say, a coupled-channels approach discussed by Singham [5].)

The second striking feature is strong sensitivity of the cross section to the mixing angle. We reported on this feature (in a different guise) in ref. 1, where we emphasized that the angular shell-model correlations had a profound effect upon the magnitude of DCX by comparing the L=S=0, L=S=1, $(1p_{\frac{1}{2}})^2$, $(1p_{\frac{3}{2}})^2$, and the Cohen-Kurath wave functions. The point was made that the angular correlations of these wave functions are vastly different. with the $1p_{\frac{1}{2}}$ case having no angular correlations and the L=S=0 wave function having very strong angular correlations. As in Fig. 1 these five wave functions are represented as five points on Fig 6. The Cohen-Kurath wave function is seen to lie about half way between the maximum and minimum values.

Also included on the Fig. 6 is a calculation which omits spin flip (note for $0^+ \rightarrow 0^+$ transitions we have assumed that both neutrons must flip spin. In cases of mixed configurations this may not be so: we are looking into this question presently). The dramatic importance of this double-flip contribution at pion energy 50 MeV was emphasized in the calculation of Bleszynski and Glauber. A similar plot for 30 MeV DCX would show much less double-spin-flip. This is to be expected because the p-wave in the pion-nucleon interaction is much weaker at lower pion energy.

In most of our calculations we have used 600 MeV/c for the off-shell range in v. Fig. 6 also shows a calculation using a different value of the off-shell range of the pion-nuclear potential. Our earlier work used a range of 300 MeV/c which is probably low at least for 50 MeV pions and partly accounted for our underestimate of the DCX cross section. At least this gives an indication of the kind of theoretical uncertainties which are present even in a model which includes only the sequential process.

If we (optimistically) assume that the theoretical error bars are of the same size as the experimental ones we can plot error bars as a band. Two ranges of mixing angles are consistent with these cross sections. One range is in the region of the Cohen-Kurath point. The second surrounds the pure $(1p_{\frac{3}{2}})^2$ configuration (near 0°). These ranges are really quite restrictive. We hope that plots like this will stimulate theorists to attempt to lower the theoretical uncertainties to make a real statement about the nuclear wave function of the target. As suggested earlier if different forms of the nuclear wave function are used (different radial dependencies or explicit short-range factors) then the relation with the simple shell-model calculations may not be possible, but more essential physics may be included.

We next compute the χ^2 for the measured angular distribution at 50 MeV as a function of the mixing angle. Fig. 7 displays $10/\sqrt{\chi^2}$ *vs.* m using the data of Ref. 12. The result shows a prominent and rather narrow peak near 60°. A peak is also present near 0°, but the corresponding angular distribution is not as satisfactory.

3.2 ^{18}O Configuration Analysis, sd-Shell Model

Fig 8. displays the forward DCX cross section for an incident 50 MeV pion *vs.* the two mixing angles. If we paint a stripe corresponding to, say, twice the experimental error bars on the sides of the mountain we would restrict the possible wave functions very strongly because of the steepness of the mountain. As with the ^{14}C case the experiment picks out a region which corresponds neither to the maximum nor minimum possible values allowed by the pure sd-shell.

The same data is presented in a contour or topographic map in Fig. 9. The experimental forward cross section is about 5.5 $\mu b/sr$ [15]. This defines a ring surrounding the mountain. The shell-model calculations mentioned earlier lie close to this region!

As with ^{14}C we now calculate the χ^2 over the full angular distribution for each of the points on the configuration map. The chi-square surface shown in Fig. 10 has two prominent minima at (θ, ϕ) of (20,100) and (70,40). Since minima are hard to see on a surface plot, we have plotted $10/\sqrt{\chi^2}$ so that the good points stick up as sharp peaks (Fig. 11). The angular distributions corresponding to the largest of these peaks are given in Fig. 12. Both give satisfactory fits to the data, although they miss the 50° data point badly. The angular distribution for a configuration point near the center of the map is also shown to give an impression of the variety of angular distributions possible with sd-shell wave functions.

We have calculated all angular distributions for an incident pion laboratory energy of 165 MeV to see if we could reproduce the celebrated minimum in the angular distribution at 20°. It does not seem to be possible without either more complex shell structure or additional reaction mechanisms.

Fig. 13 gives a similar topographic χ^2 plot for 292 MeV. (The data was read by eye from the small graphs in Ref. 16) While the general structure of the plot is quite similar to that at 50 MeV, the preferred points have drifted together. This unsatisfactory state of affairs could result from a general overprediction of our high-energy DCX cross sections. The chi-squared procedure compensates for this by choosing a less correlated wave function. Whether this is due to our approximate treatment of recoil corrections, the omission of some important mechanism, or completely different reason is under study. In any case the general structure of the plot is qualitatively similar to the 50 MeV results.

3.3 ^{14}C Configuration Analysis, psd Shells Model

Fig 14 displays the topography for forward DCX in ^{14}C at 50 MeV in the psd basis. The axes are $1p_{\frac{3}{2}}$ (polar) and $1p_{\frac{1}{2}}$ *vs.* (ds) shell as the azimuthal axis. The cross sections again track the correlation plot of Fig. 4 rather closely. The next two figures show $10/\sqrt{\chi^2}$ *vs.* configuration for a full angular distribution. There are two rather high peaks, one at $(\theta, \phi) = (60, 0)$ (whose other half is at (120,0)), and the other near the center of the plot at about (100,120).

One of the peaks is just the Cohen-Kurath solution, nearly a pure p-shell! This peak appears on the edge of the plot and so is split into two half-peaks, one at (60,0) and the other at (180,120). (It is important to note that the resolution of these plots is rather coarse; θ is gridded in steps of 10° and ϕ in steps of 20°. Any structure having finer resolution than this is a figment of the gridding process.) From present data at this energy we are unable to distinguish between this and the second peak at (120,80). Additional data is necessary to resolve this ambiguity. The analysis is reminiscent of the ambiguities in a phase-shift analysis. There may be several sets of phase shifts which are consistent with a relatively small data set. One may be real, but the others are phantoms to be exorcised by additional data...taken over a wider data set or over several energies. If no point on the plot is consistent with the data then either the reaction theory is deficient or we have used an insufficient data set.

Angular distributions corresponding to three best candidates are plotted in Fig. 17 along with data from Ref. 12. They are somewhat reasonable. but all miss the 130° point rather badly. Also included on the plot are angular distributions corresponding to two other points. One corresponds to a configuration for which there is very close pairing (as determined by Fig. 5). This calculation yields a huge forward-peaked cross section. The last curve was produced from a configuration in which the nucleons avoid each other; the cross section has a strong backward peak. It is amazing how much variation is obtainable from such a simple sequential model and such a primitive shell structure.

The oscillator parameter used to calculate these figures is fairly conventional (b=1.73 fm), but would be too small to give a rms radius consistent with the binding energy of the last neutron. To test the sensitivity of the results to this parameter the calculation was redone with a larger value (b=1.83 fm). The actual sizes of the cross sections decrease somewhat, but the general form of the topographic plot is essentially unaltered. The Cohen-Kurath and central peaks are still present.

Figure 18 is a plot derived from the 30 MeV data [12]. These data consists of only four angular points, and are less constraining. Again the data demands that we include points near the Cohen-Kurath point. The highest peak is at (60,20) is, at our present resolution, only barely distinguishable from that at (80,0). The central maximum which appeared in the 50 MeV data seems to be weaker: it's a good bet that it was a phantom solution.

3.4 ^{42}Ca with Configuration Mixing

Finally we present calculations of DCX on ^{42}Ca. In addition to the pure $1f_{\frac{7}{2}}$ shell result we have also included results from an extended basis which includes $1f_{\frac{7}{2}}$, $1p_{\frac{1}{2}}$ and $1p_{\frac{3}{2}}$ configurations. The results, using coefficients derived from the computer program Oxbash [17] and provided to us by J. Ginocchio, are presented in Fig. 19 and 20. The Kuo-Brown, Wildenthal, and FPY interactions give fairly consistent predictions, all about 50 percent higher than a pure $1f_{\frac{7}{2}}$ model. The calculations which include configuration mixing are remarkably consistent with the data at 35 MeV [18]. The effect of configuration mixing in ^{42}Ca is in general agreement with the calculations of Ref. 19, but lie nearly a factor of two above the data at 292 MeV [20]. This once again points out a deficiency in the reaction theory that we have used.

4 CONCLUSIONS

We have presented an exploratory configuration analysis of nuclear wave functions using DCX. The distorted waves used are calculated from a finite-range optical model which is in approximate agreement with elastic and with SCX data. Only the sequential mechanism has been included. By comparing our predictions of all possible configurations within a given basis we have seen that the existing experimental data essentially excludes most configurations, assuming the validity of the reaction theory. This is a risky assumption, but believe that the roughly consistent results are extremely provocative. We intend to attempt a similar analysis which also contains meson exchange currents and short-range correlations.

We recommend others try such analyses with their own dynamical models. The analysis may be carried out not for DCX in isolation, but in conjunction with SCX, elastic, inelastic, and other reactions which may be described by the same nuclear wave functions and pion distorted waves.

REFERENCES

1. Proceedings of the LAMPF Workshop on Pion Double Charge Exchange, edited by H. Baer and M. Leitch, Los Alamos National Laboratory Conference Proceeding LA-10550-C (1985).

2. W. Gibbs, W. Kaufmann, P. Siegel, The ABC's of Pion Charge Exchange, Ref. 1, p. 90.

3. M. Bleszynski and R. Glauber, Phys. Rev. **C36**, 681 (1987).

4. Proceedings of the Second LAMPF Workshop on Pion Double Charge Exchange, Los Alamos, Aug. 14-18, 1989, to be published.

5. S. Cohen and D. Kurath, Nucl. Phys. **73**, 1 (1965).

6. E. Halbert, J. McGrory, B. Wildenthal, and S. Pandya, Adv. Nucl. Phys. **4**, 315 (1971).

7. R. Lawson, Theory of the Nuclear Shell Model, Clarendon Press, Oxford (1980). See Eqn. 1.61.

8. H. T. Fortune and G. Stephans, Phys. Rev. **C25**, 1 (1982).

9. N. Auerbach, W. Gibbs, J. Ginocchio, and W. Kaufmann, Phys. Rev. **C38**, 1277 (1988).

10. J. Ginocchio, The Effect of Configuration Admixtures on Pion Double Charge Exchange, Los Alamos Preprint LA-UR-89-2086 (1989). See especially the Appendix.

11. W. Kaufmann and W. Gibbs, Phys. Rev. **C28**, 1286 (1983).

12. M. Leitch, H. Baer, R. Burman, C. Morris, J. Knudson, J. Comfort, D. Wright, R. Gilman, S. Rokni, E. Piasetzky, Z. Weinfeld, W. Gibbs, and W. Kaufmann, Phys. Rev. **C39**, 2356 (1989). ^{14}C several low energies. For the 50 MeV data see M. Leitch, E. Piasetzky, H. Baer, J. Bowman, R. Burman, B. Dropetsky, P. Gram, F. Irom, R. Roberts, G. Rebka, J. Knudson, J. Comfort, V. Pinnick, D. Wright, and S. Wood, Phys. Rev. Lett. **54**, 1482 (1985).

13. P. Siegel and W. Gibbs, Phys. Rev. **C33**, 1407 (1986).

14. G. Rowe, M. Salomon, and R. Landau, Phys. Rev. **C18**, 584 (1978).

15. A. Altman *et al.* Phys Rev. Lett. **55**, 1273 (1985). ^{18}O 50 MeV

16. S. Greene, W. Braithwaite, D. Holtkamp, W. Cottingame, C. Moore, G. Burleson, G. Blanpied, A. Viescas, G. Daw, C. Morris, and H. Thiessen, Phys. Rev. **C25**, 927 (1982). ^{18}O 292 MeV

17. A. Etchegoyen, W. Rae, N. Godwin, and B. Brown, Michigan State Cyclotron Laboratory Report 524 (1985).

18. Z. Weinfeld, E. Piasetzky, H. Baer, R. Burman, M. Leitch, C. Morris, D. Wright, S. Rokni, and J. Comfort, Phys. Rev. **C37**, 902 (1988) and Z. Weinfeld, E. Piasetzky, M. Leitch, H. Baer, C. Mishra, J. Comfort, J. Tinsley, and D. Wright, Los Alamos Preprint (1989) ^{42}Ca data at 35 MeV

19. E. Bleszynski, M. Bleszynski, and R. Glauber, Phys. Rev. Lett. **60**, 1483 (1988).

20. K. K. Seth, M. Kaletka, S. Iverson, A. Saha, D. Barlow, D. Smith, and L. C. Liu, Phys. Rev. Lett. **52**, 894, (1984). ^{42}Ca data at 292 MeV.

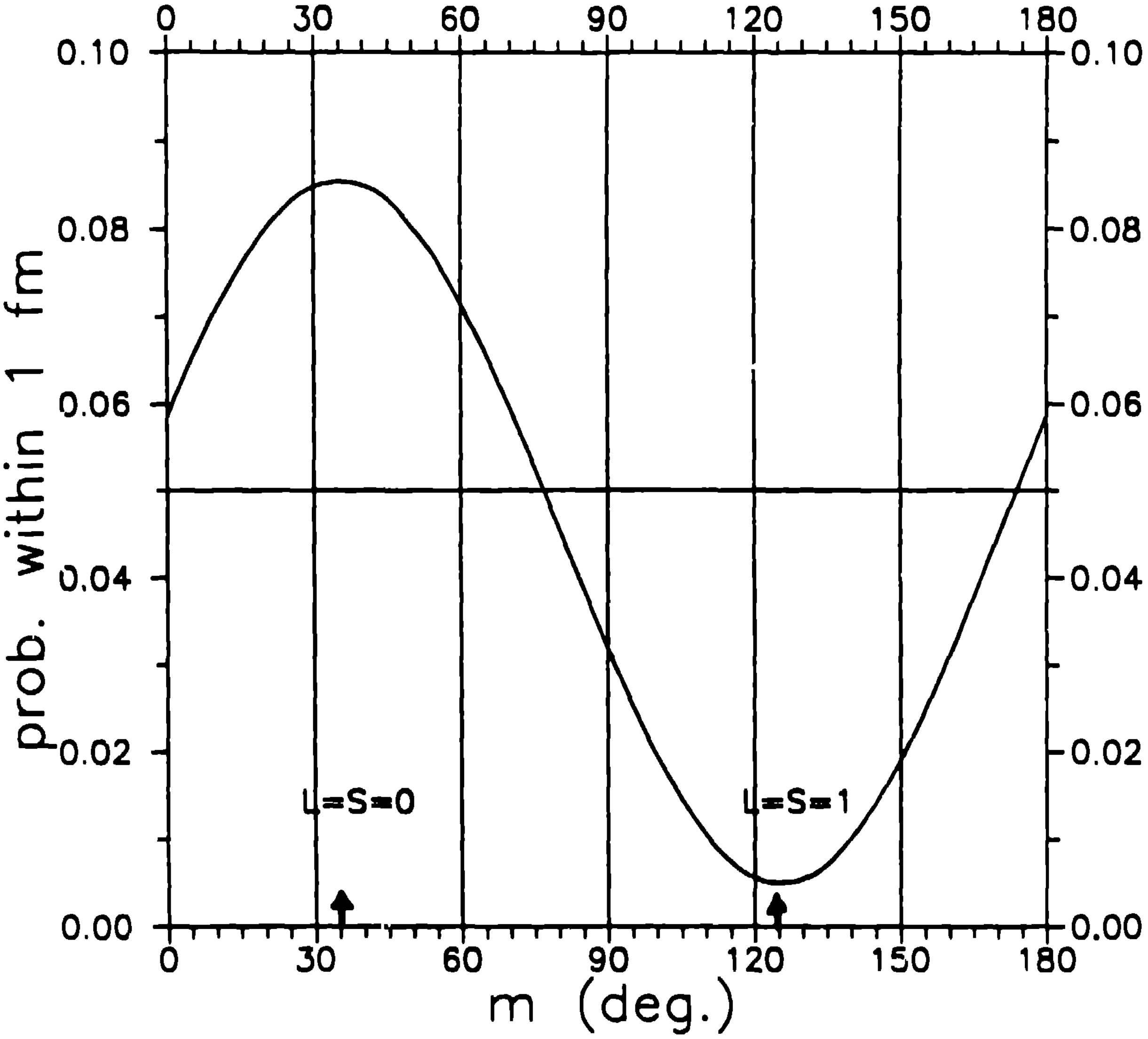

Correlation Map for p-shell ^{14}C. m is the mixing angle between the $(1p_{3/2})^2$ and $(1p_{1/2})^2$ components. The first nucleon is placed at 2 fm. from the origin. The y-axis denotes the probability that the second nucleon is within 1 fm. of the first.

Figure 1.

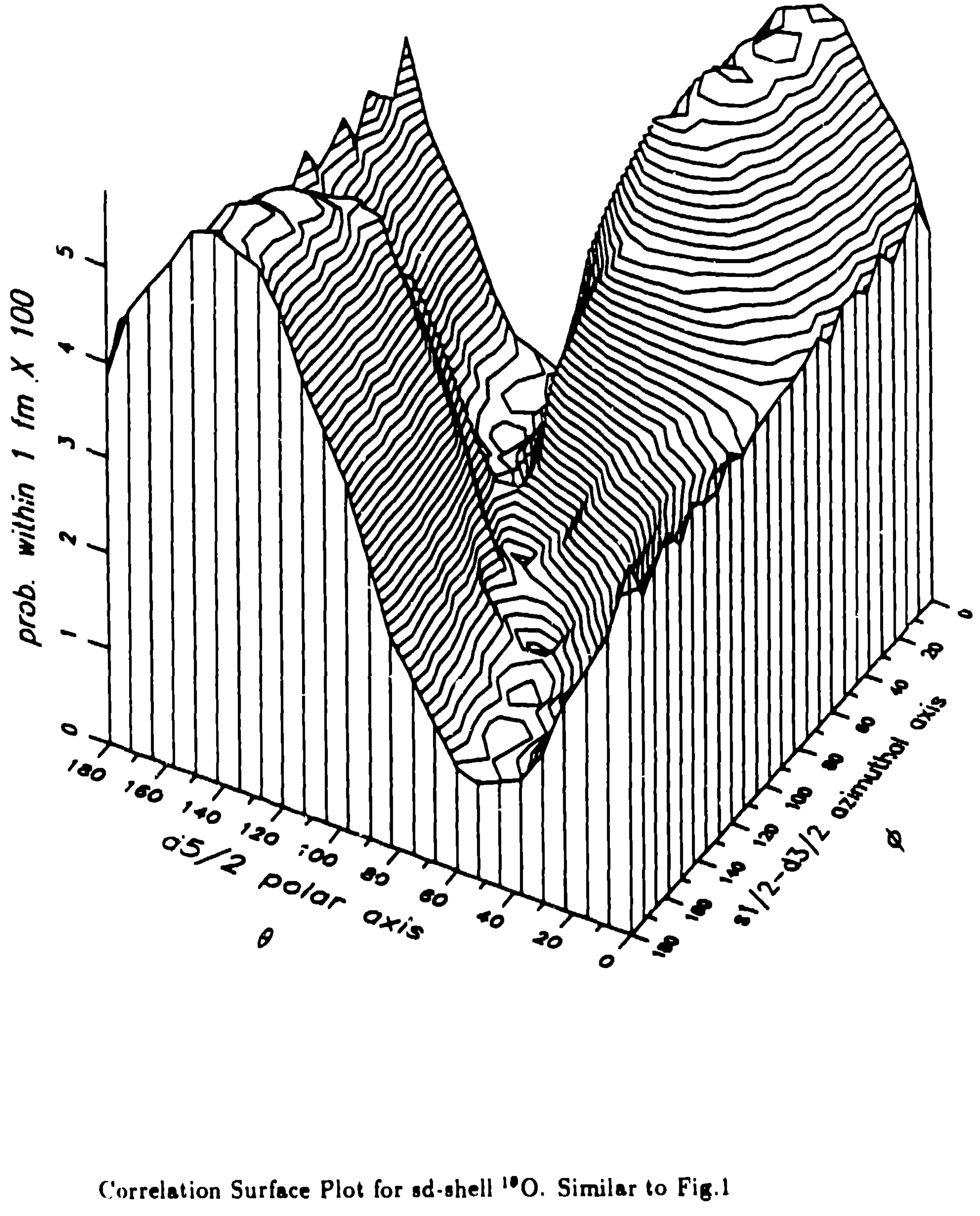

Correlation Surface Plot for sd-shell ^{18}O. Similar to Fig.1

Figure 2.

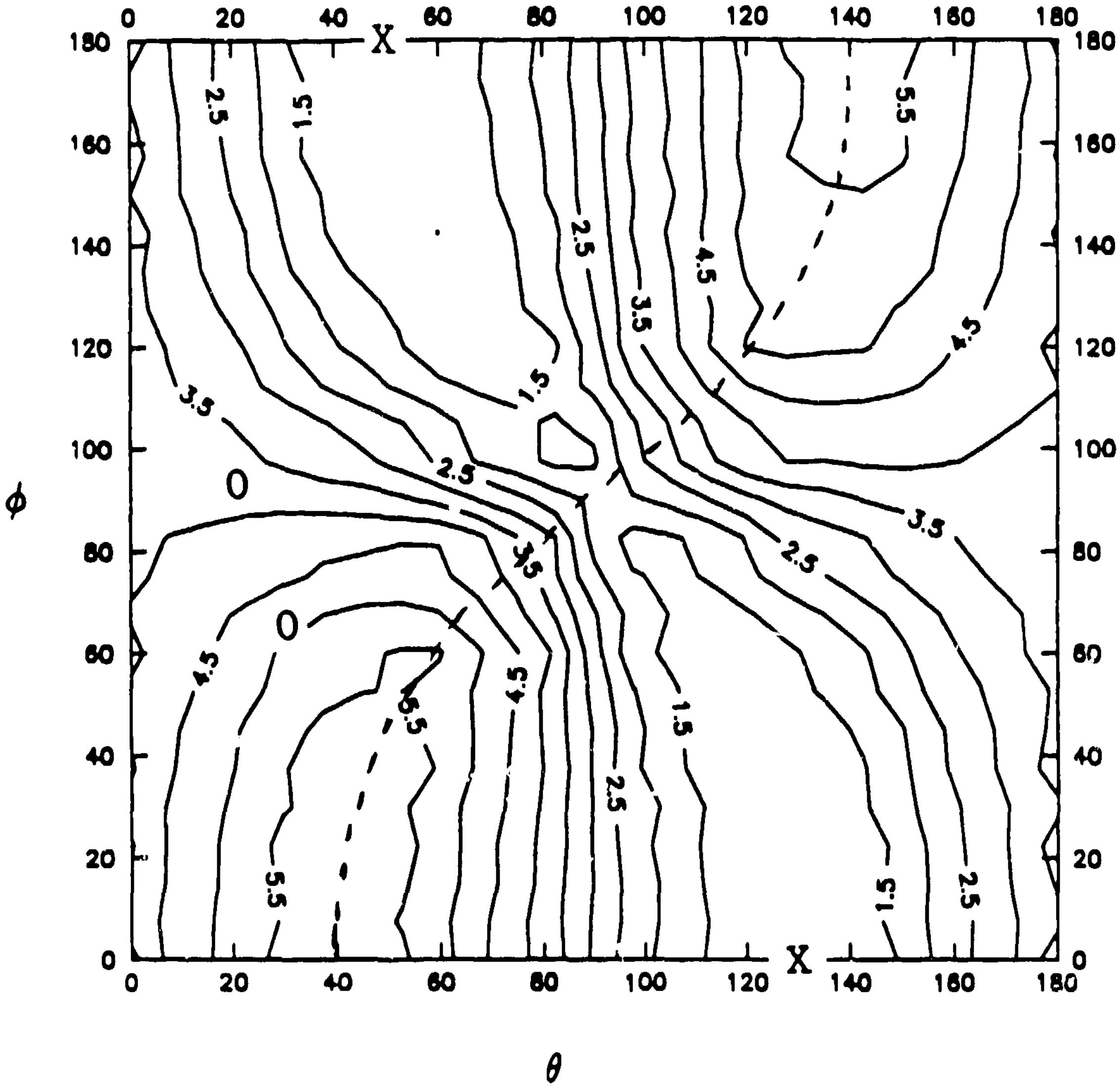

Correlation Topological Map for sd-shell ^{18}O. Fig. 2 expressed as topological plot. The contours are labelled as probability times 100 of the second particle being within 1 fm of the first. The line sketched across the plot gives the line on which L=S=0. The crosses on the border give the L=S=1 state. Two shell-model points as described in the text are indicated on the plot.

Figure 3.

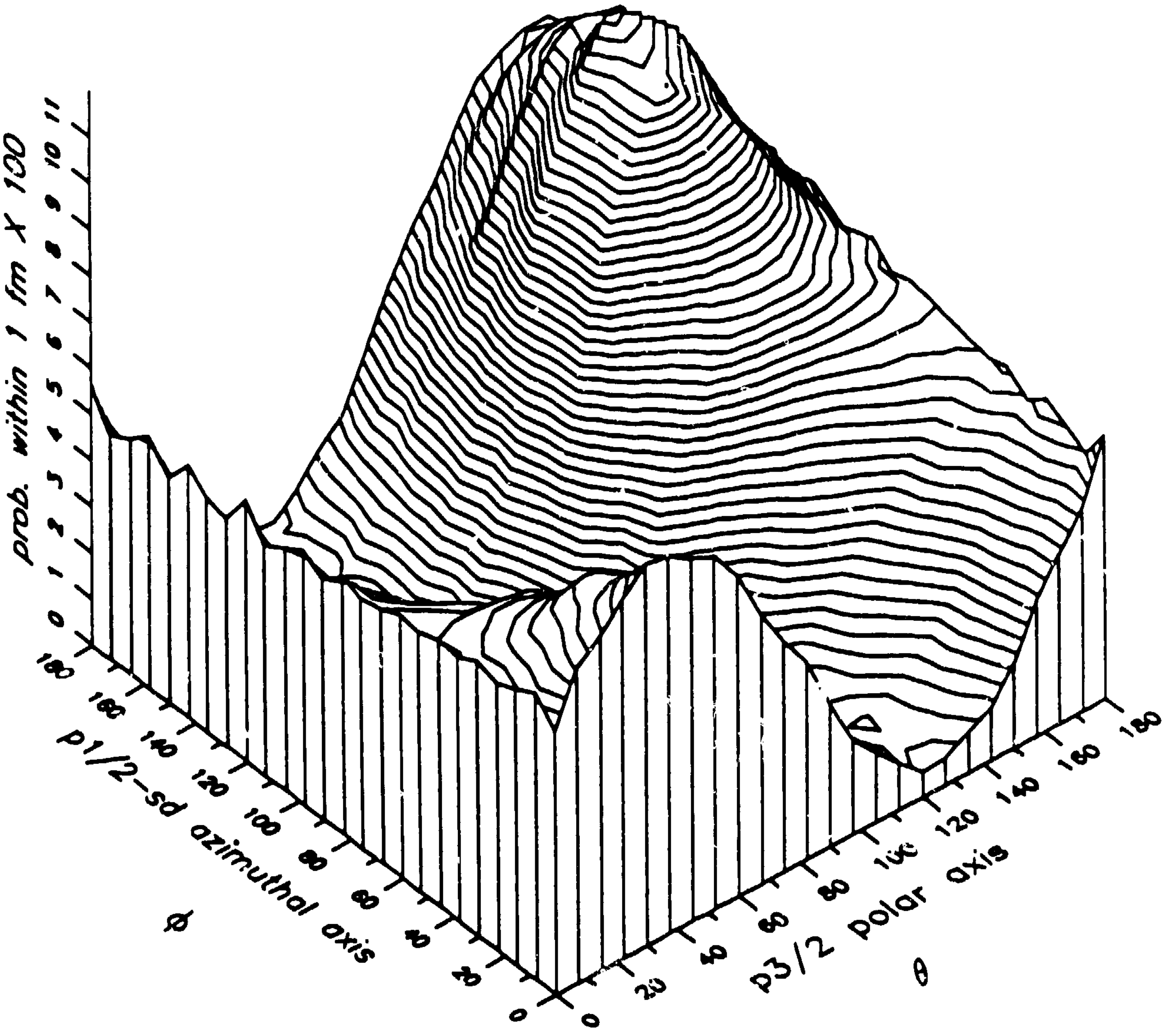

Correlation Surface Plot for p-, sd-shell ^{14}C. The huge 'correlation summit' shows that in this extended model very strong nucleon-nucleon correlations are possible. The pure p-shell model result of Fig. 1 may be seen on the boundary of the surface alone the line of longitude $\phi = 0$ or $\phi = \pi$.

Figure 4.

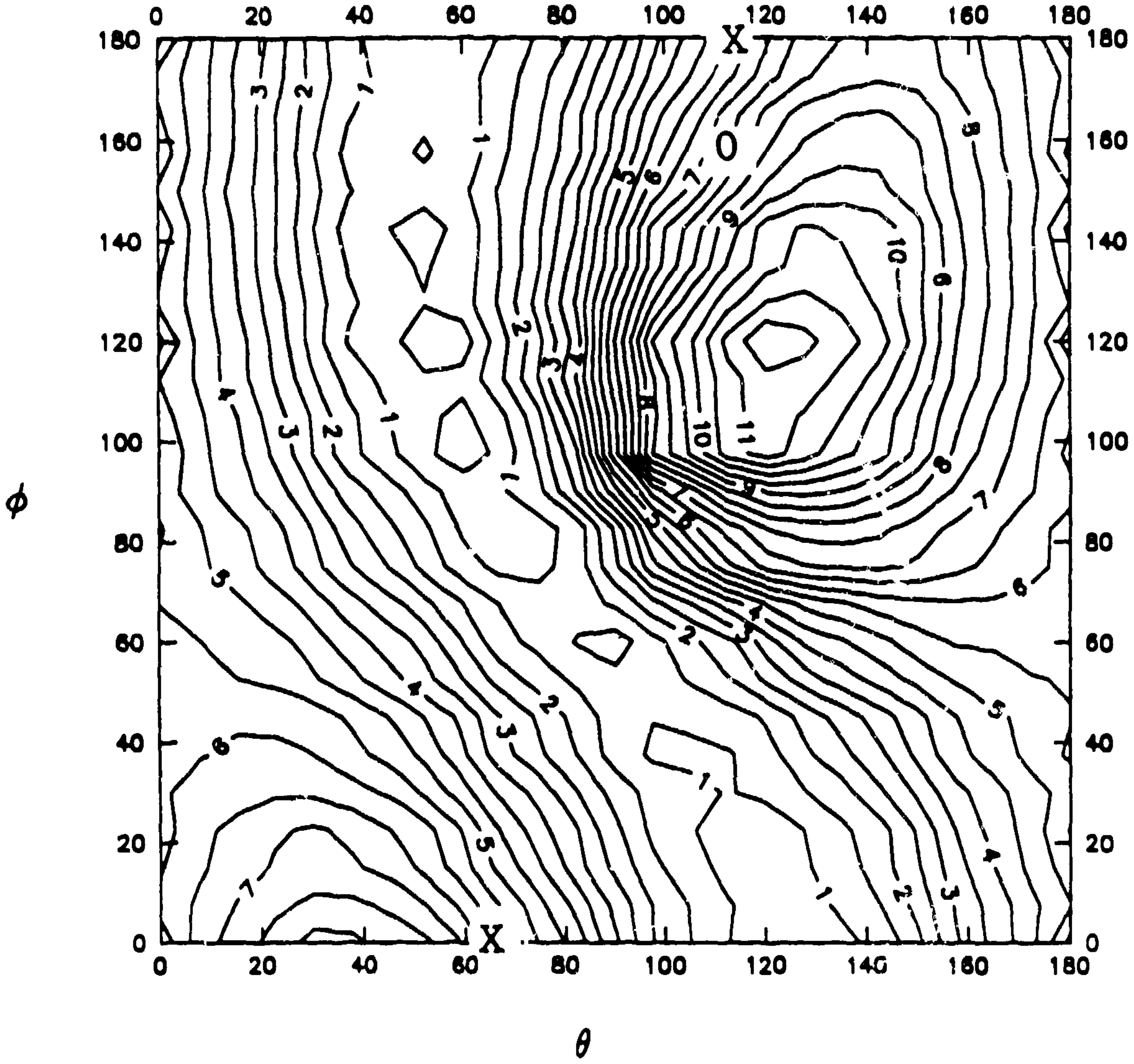

Correlation Topological Map for p-, sd-shell ^{14}C. The Cohen-Kurath [5] and Fortune-Stephans [8] shell models are shown on the map. Note the correlation summit near $\theta = \phi = 120°$.

Figure 5.

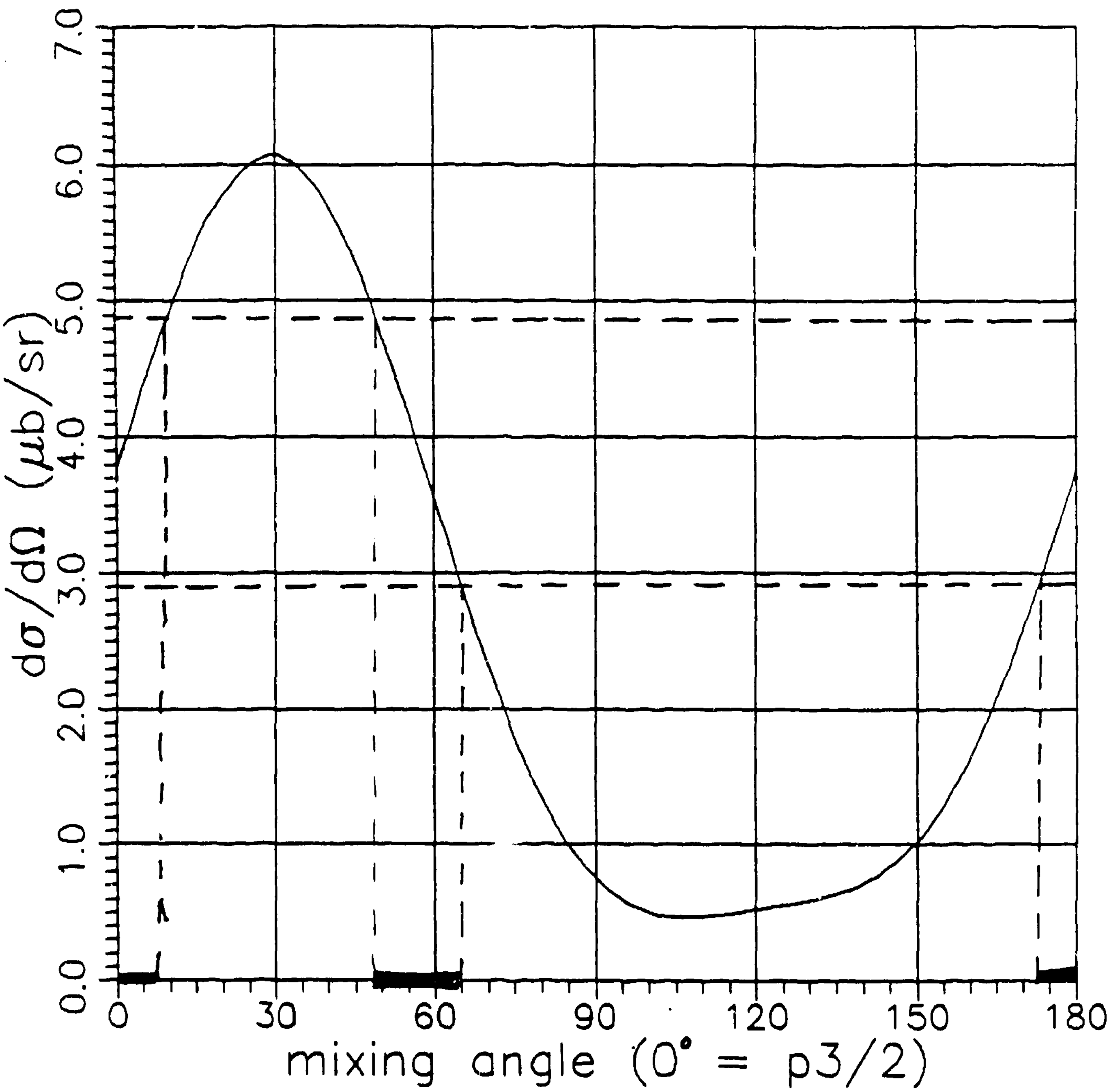

Forward Cross Section for DCX on ^{14}C at 50 MeV in a pure p-shell model. The oscillator wave function has oscillator parameter 1.73 fm. The off-shell pion-nucleon range is 700 MeV/c. Note the similarity to Fig. 1. The horizontal band is centered about the experimental forward DCX [12] and has a width twice the experimental error. It is seen to sharply restrict the possible values of the mixing angle m to two intervals about 0 and about 60°.

Figure 6.

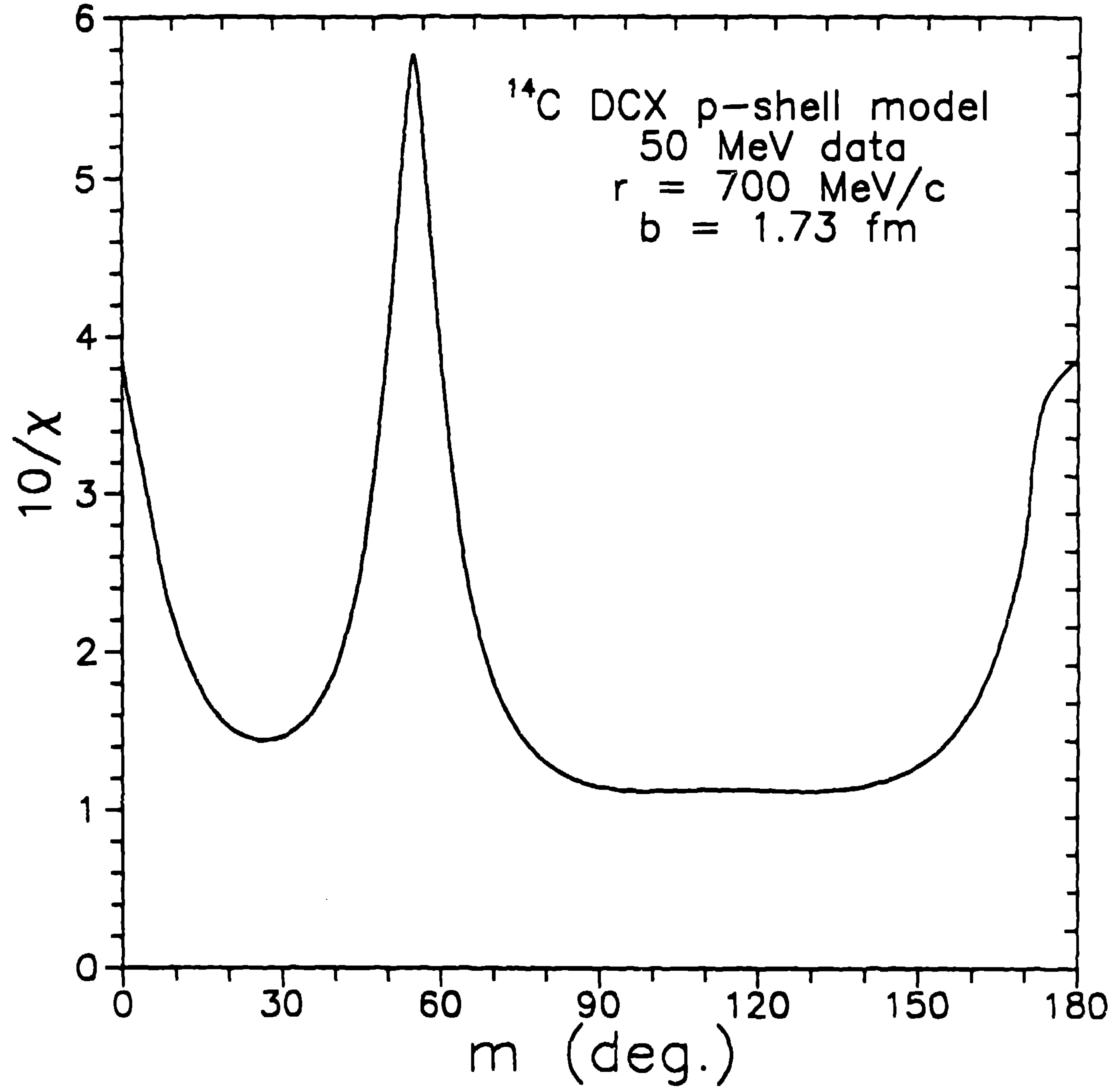

$10/\sqrt{\chi^2}$ for full angular distribution (Data from Ref. [12]) at 50 MeV. The angular distribution favors the peak near 60° over that near 0°.

Figure 7.

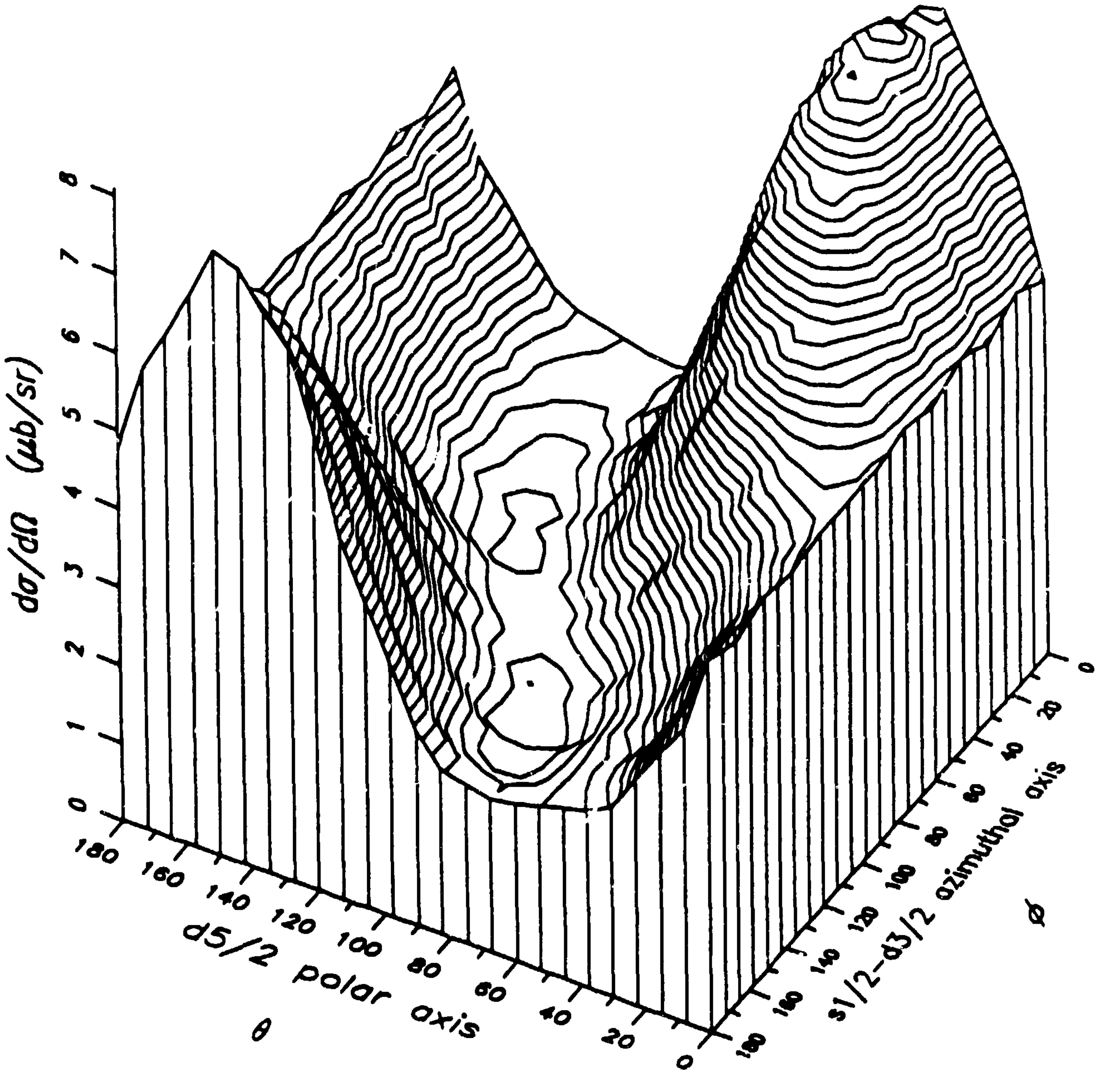

The forward cross section for DCX on ^{18}O at 50 MeV in a sd-shell model. The experimental forward cross section of about 5.5 $\mu b/sr$ [15] is on the steep slopes of the mountain. Note the strong similarity to Fig. 2.

Figure 8.

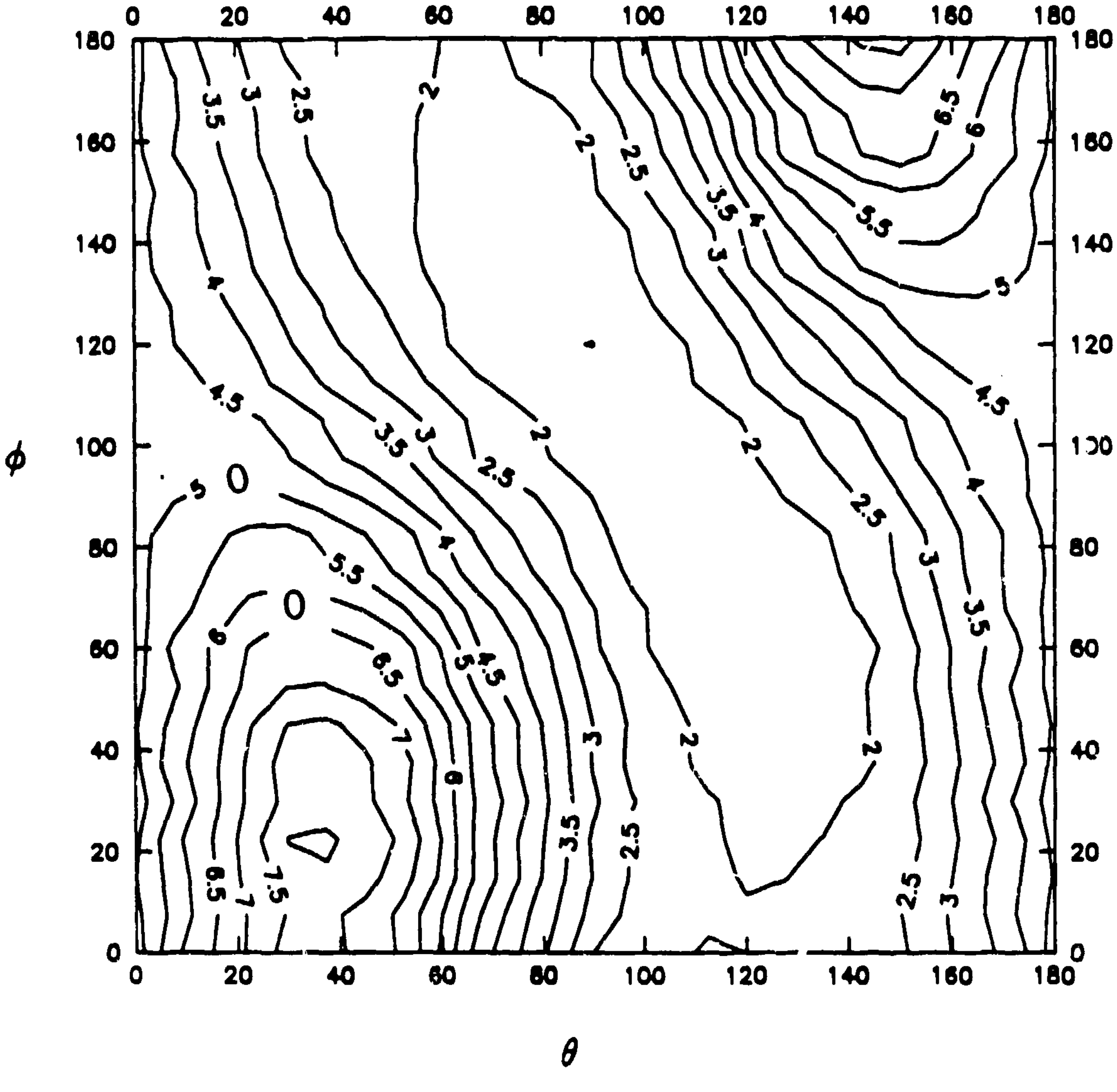

The topological map corresponding to Fig. 8. The two shell model points are reproduced on this plot. Note that they bracket the experimental forward cross section.

Figure 9.

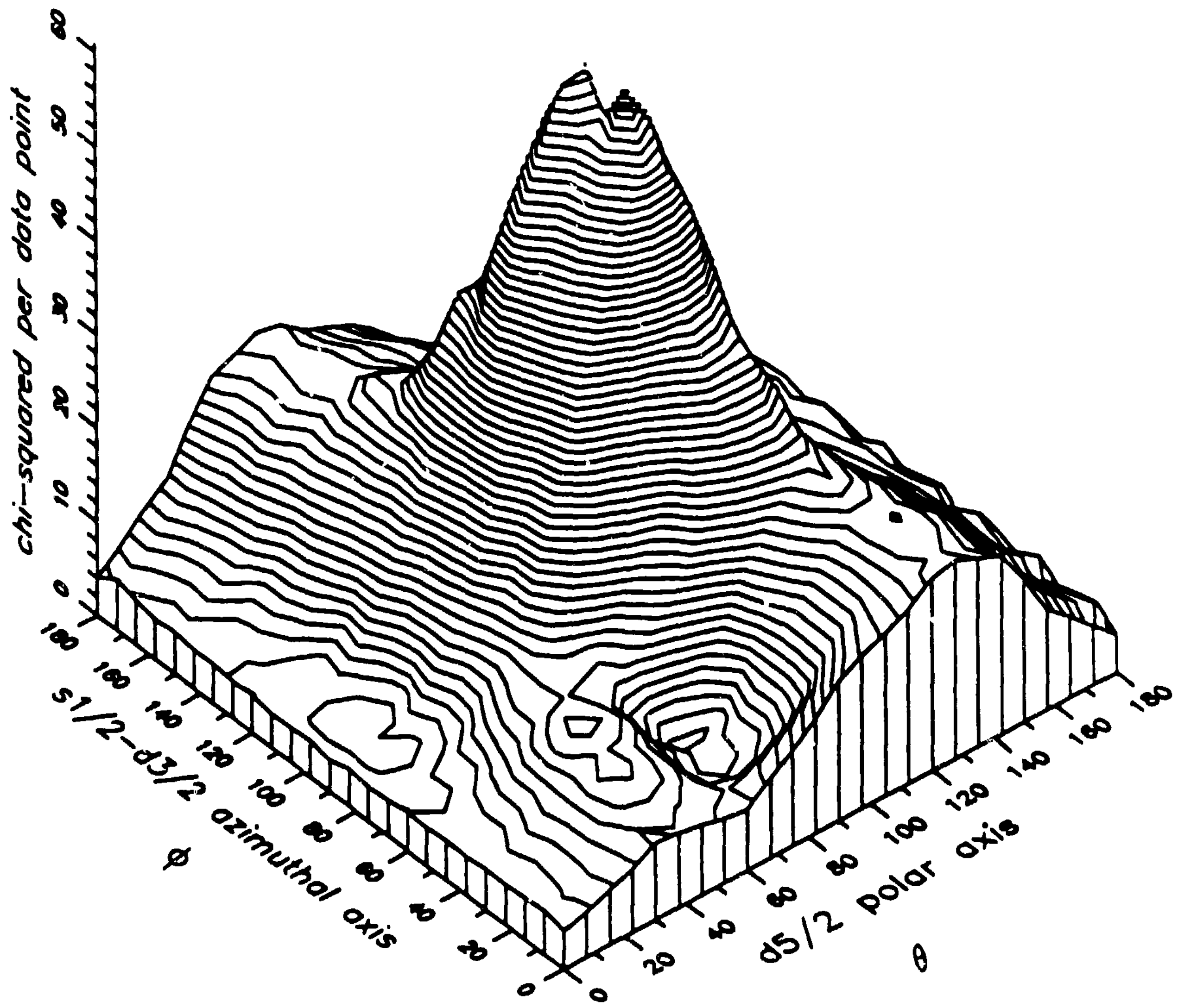

χ^2 per data point for the full angular distribution in ^{18}O at 50 MeV. the two holes correspond to the 'best' angular distributions.

igure 10.

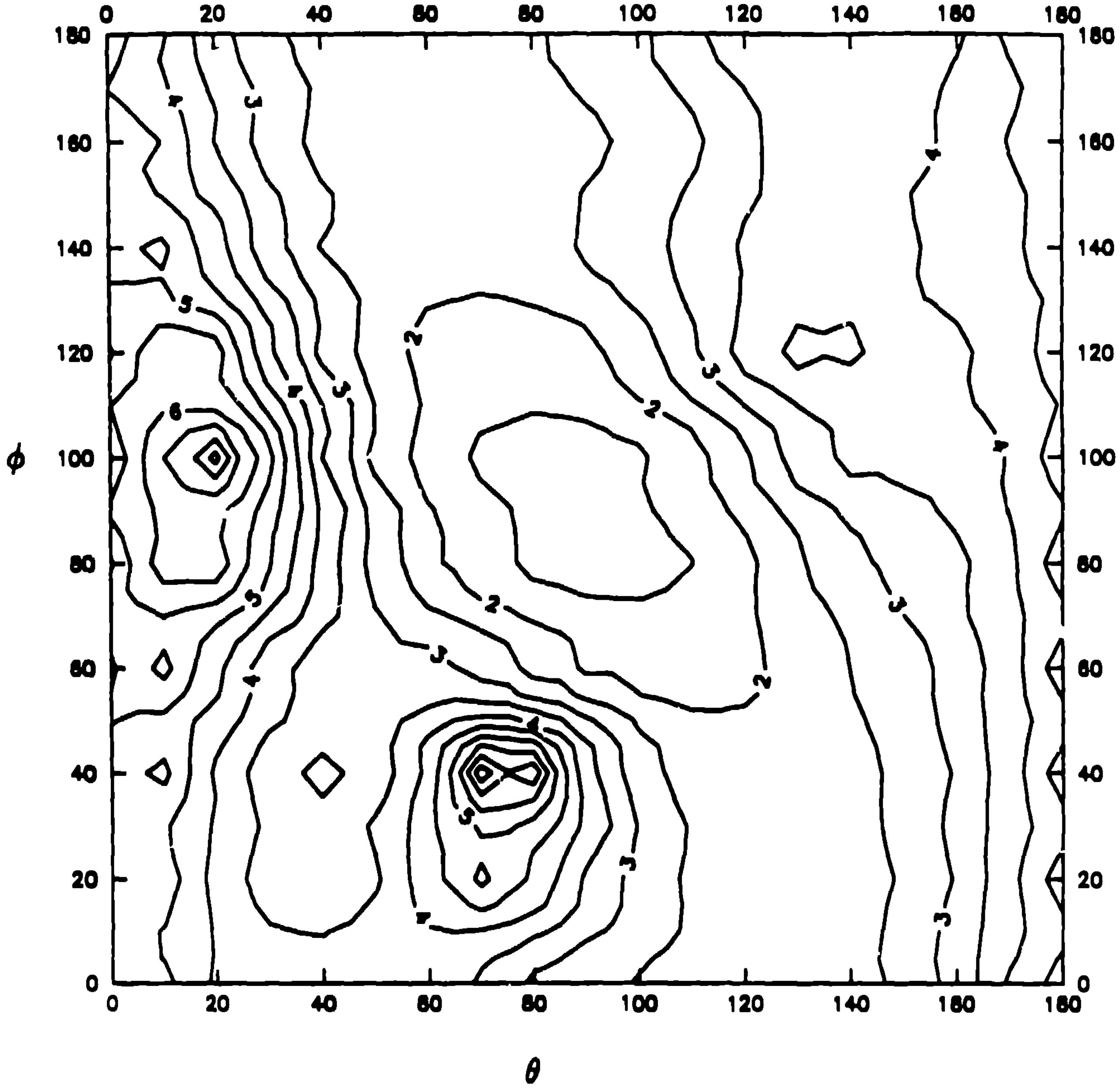

A topological map corresponding to Fig. 10. The contour lines correspond to $10/\sqrt{\chi^2}$. The angular destribution strongly prefers two regions near (θ,ϕ) of (20,100) and (70,40). In this and all other topological maps of $10/\sqrt{\chi^2}$ the calculations were performed in steps of 20° in ϕ and 10° in θ. Finer structures than this are merely figments of the gridding process.

Figure 11.

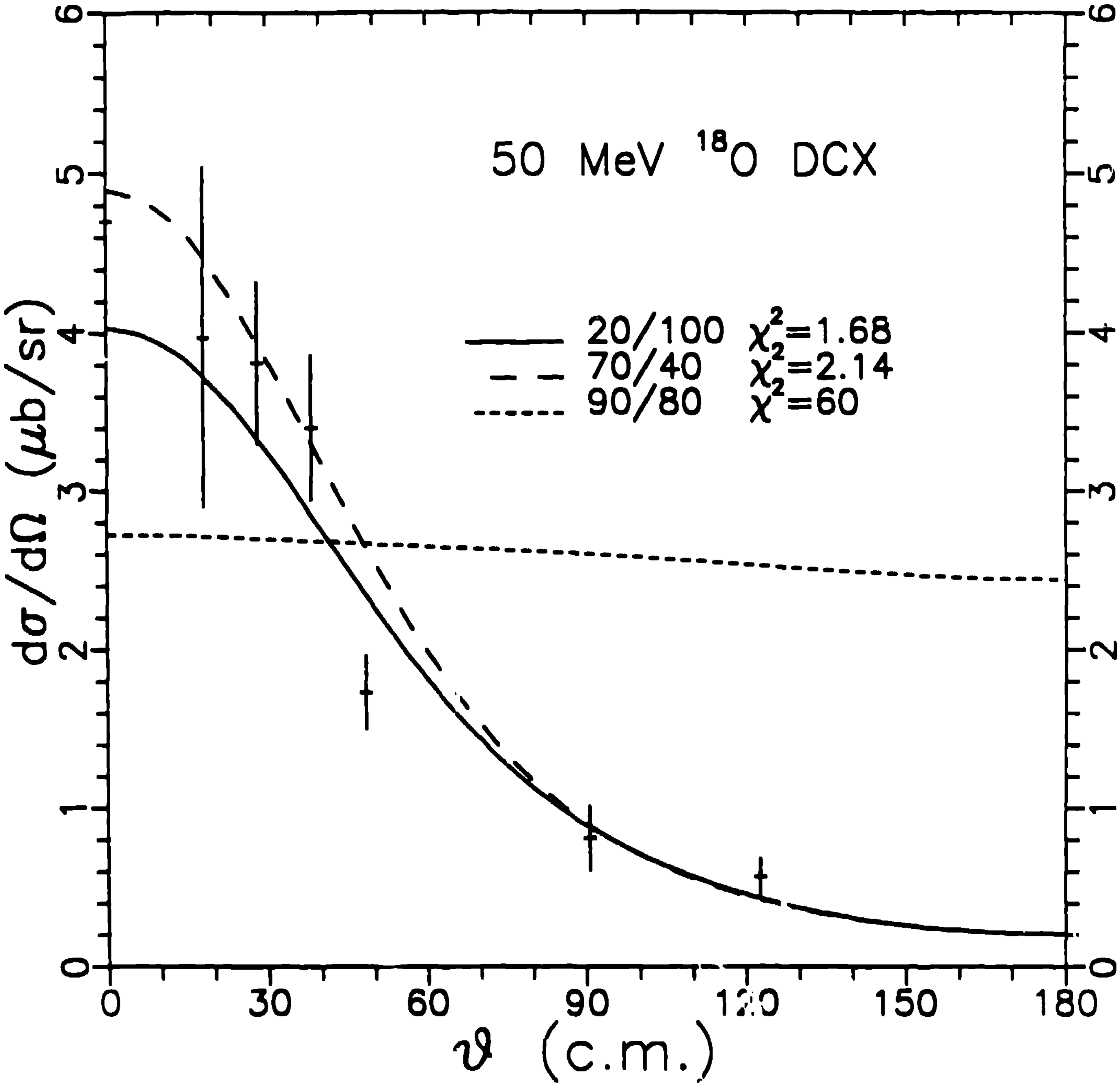

The angular distributions of the two best solutions in Fig. 11. Also included is an angular distribution taken from one of the regions rejected by the $10/\sqrt{\chi^2}$ criterion. One can do remarkably poorly with the wrong nuclear structure.

Figure 12.

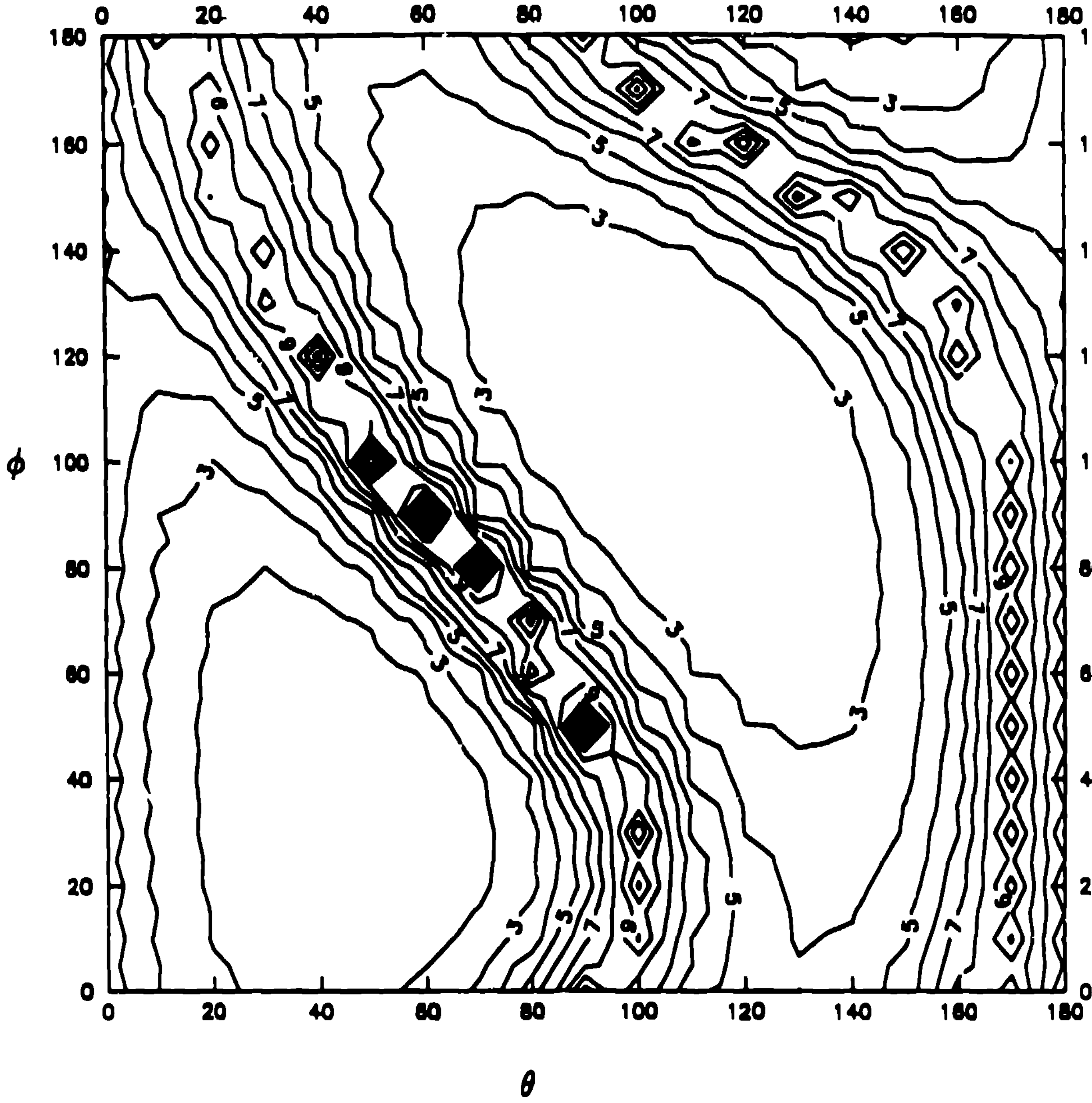

A topological map of $10/\sqrt{\chi^2}$ for ^{18}O DCX at 292 MeV. The data is from [16]. The two solutions of Fig. 9 still appear, but they have moved somewhat which suggests that we do not yet have the proper energy dependence in the reaction theory.

Figure 13.

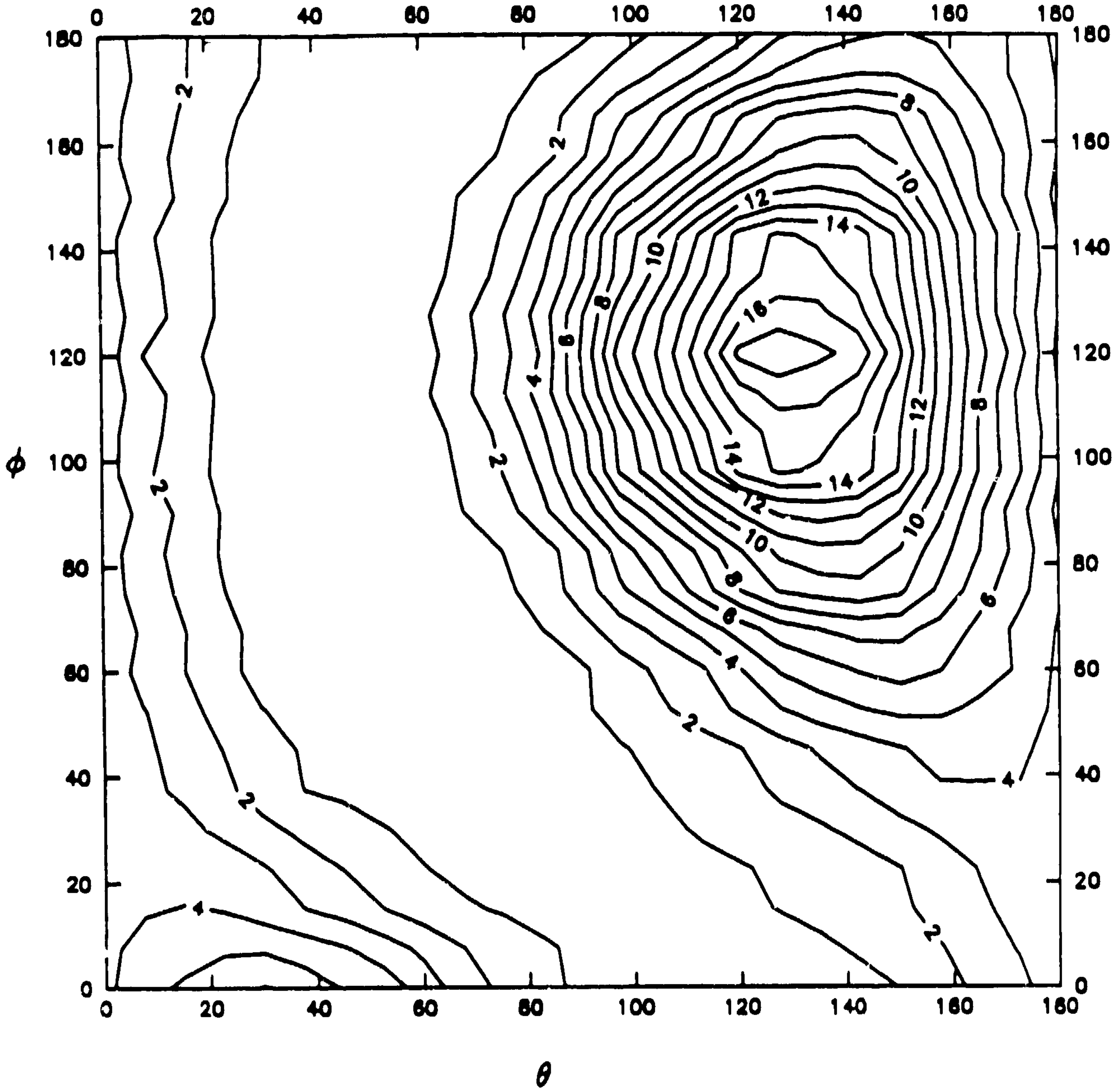

Forward cross section for DCX on ^{14}C at 50 MeV using the p- sd- shell nuclear structure. The experimental forward cross section is about 3.9 $\mu b/sr$. The immense cross sections near (120,120) mirror the high correlations seen in Fig. 4

Figure 14.

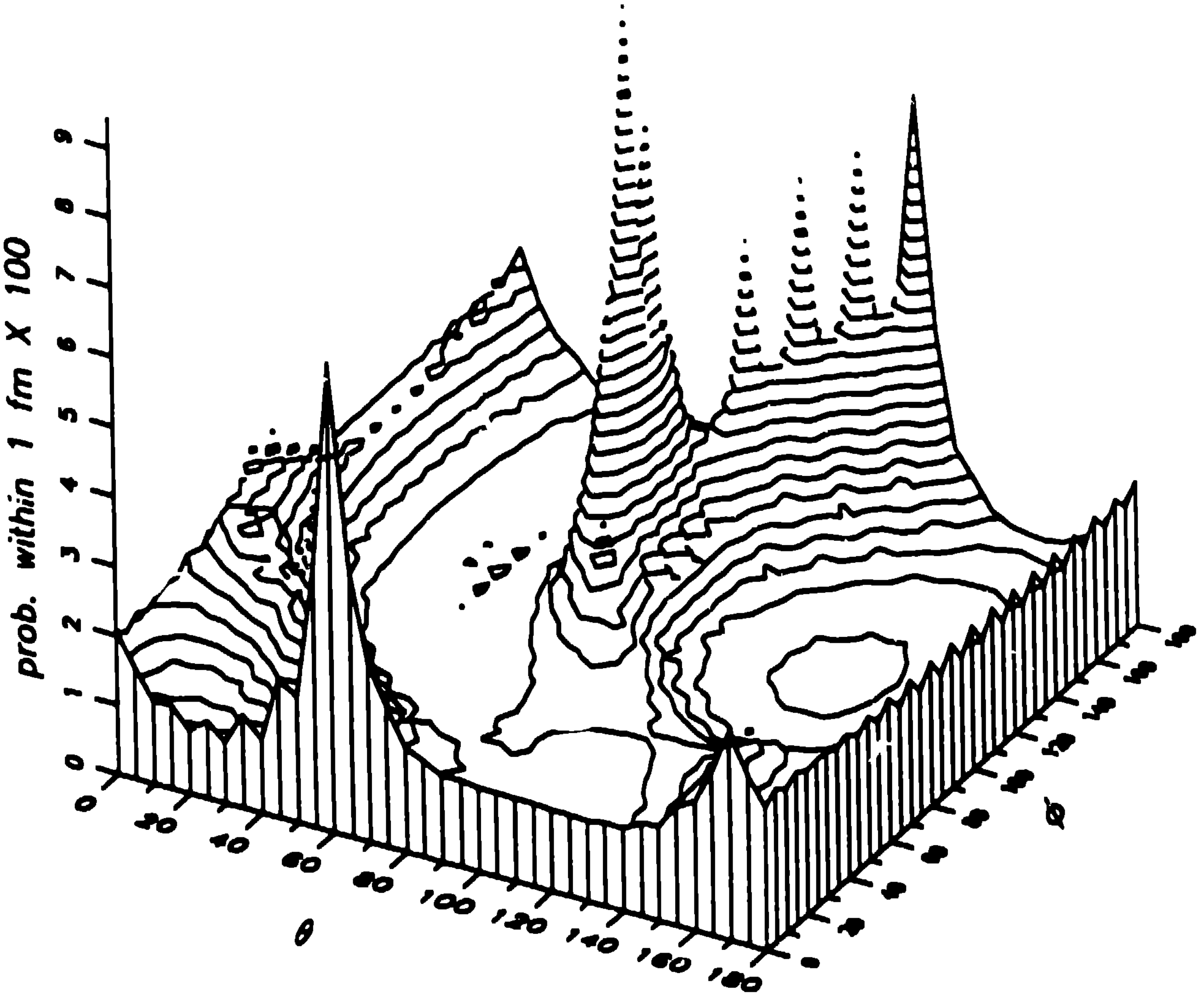

The surface map of $10/\sqrt{\chi^2}$ defined by the full angular distribution for DCX on ^{14}C at 50 MeV. The possible configurations are strongly constrained near the two shell model values and near (80,120).

Figure 15.

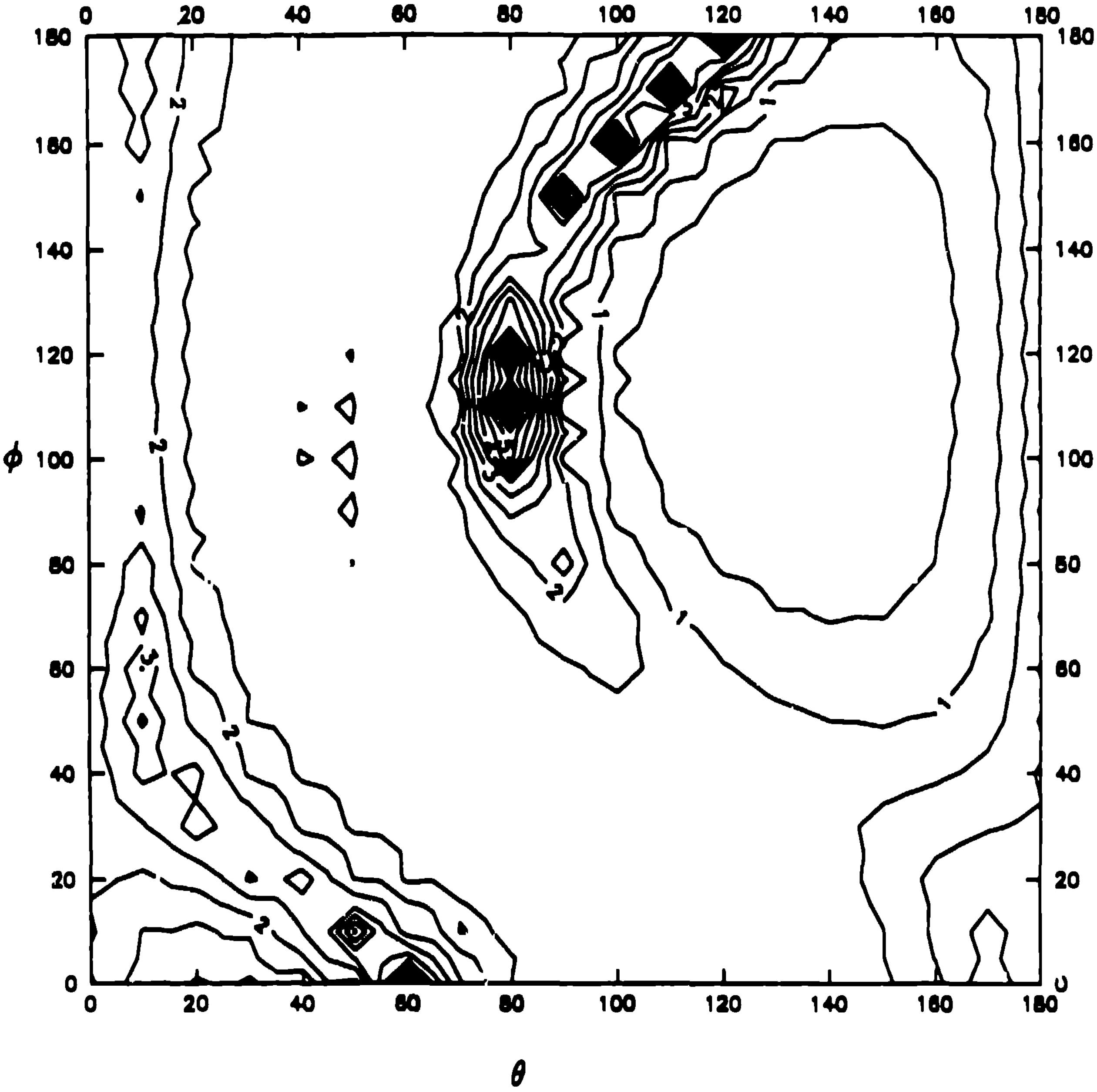

The topological map corresponding to Fig. 15. Note that the peak at (0,60) and (120,180) are the same point.

Figure 16.

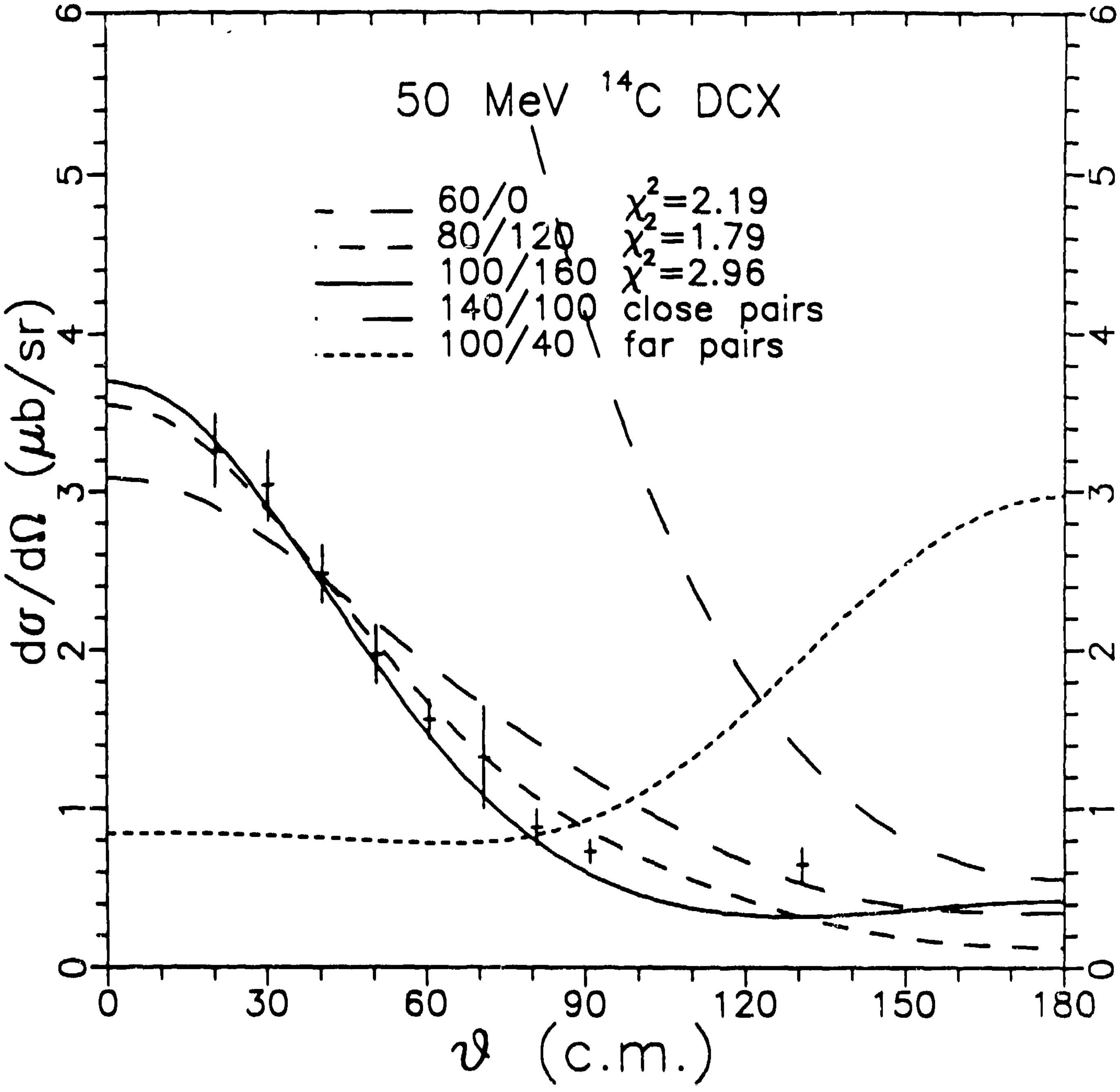

Angular distributions of the 'best' and 'worst' configurations of Fig. 16. The 'worst' correspond to both highly correlated and anticorrelated configurations.

Figure 17.

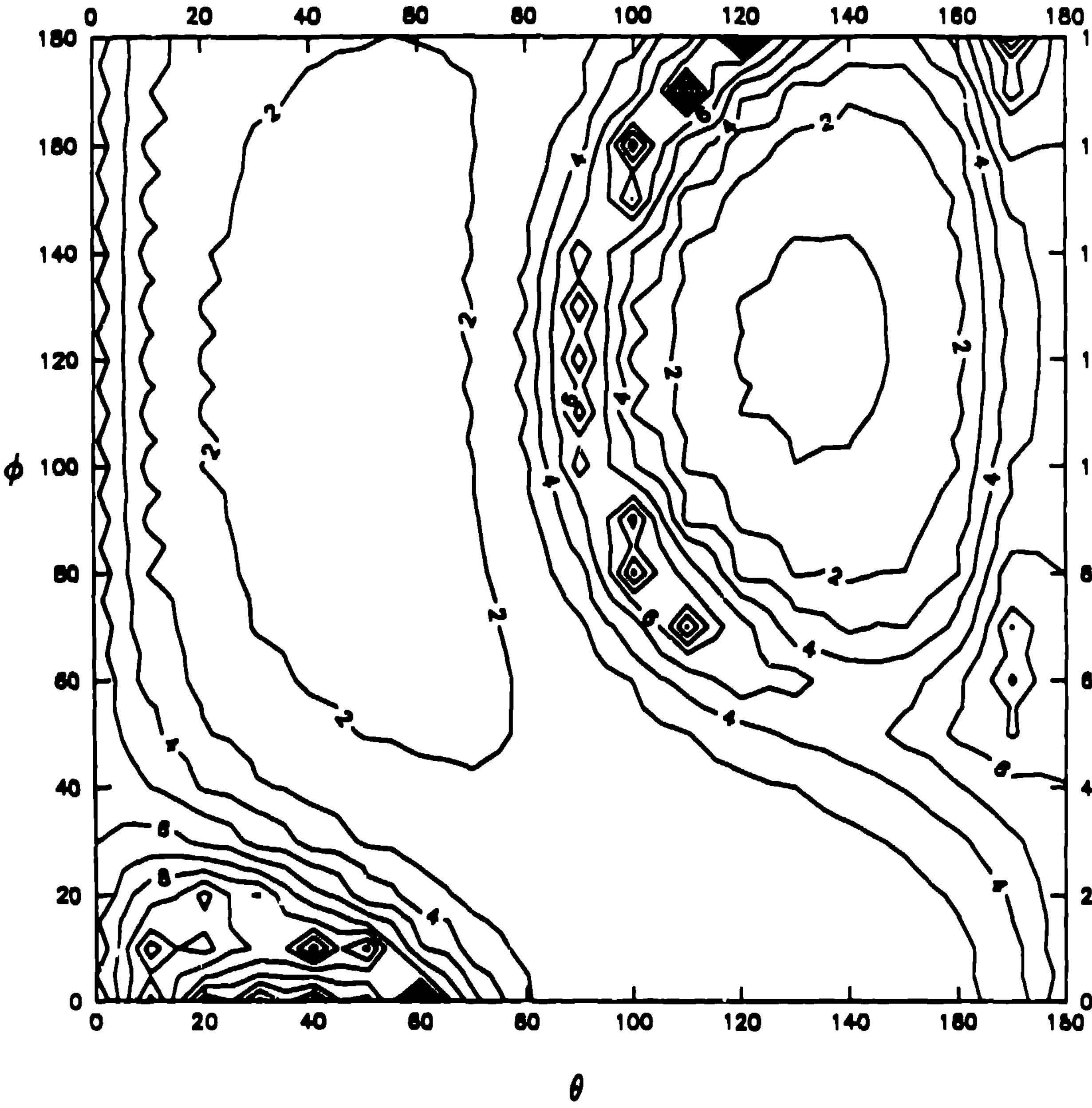

The surface map of $10/\sqrt{\chi^2}$ for ^{14}C at 30 MeV using the p- sd- shell model. The region near the Cohen-Kurath point is still a viable solutions. Note the absence of the large central peak seen in Fig. 15. Again we warn the reader that the gridding on these figures is somewhat coarse.

Figure 18.

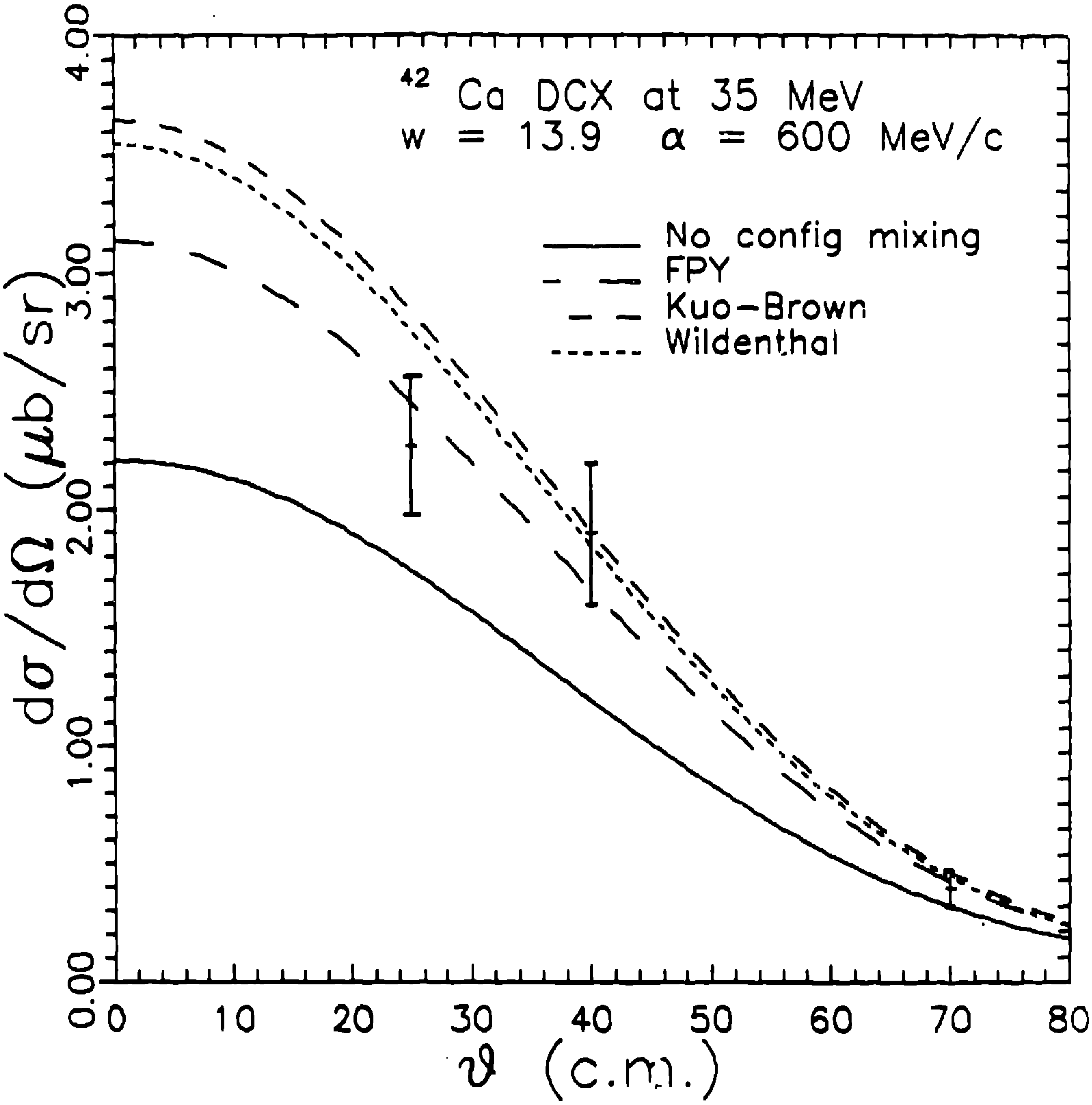

Angular distribution for DCX on ^{42}Ca at 35 MeV. The data is from [17]. Several models of configuration mixing are given. They give rather similar results. The pure $1f_{\frac{7}{2}}$ shell result is shown for comparison. W is the absorption parameter defined in Ref. 12. Its numerical value is scaled by A^2 from that of ^{14}C.

Figure 19.

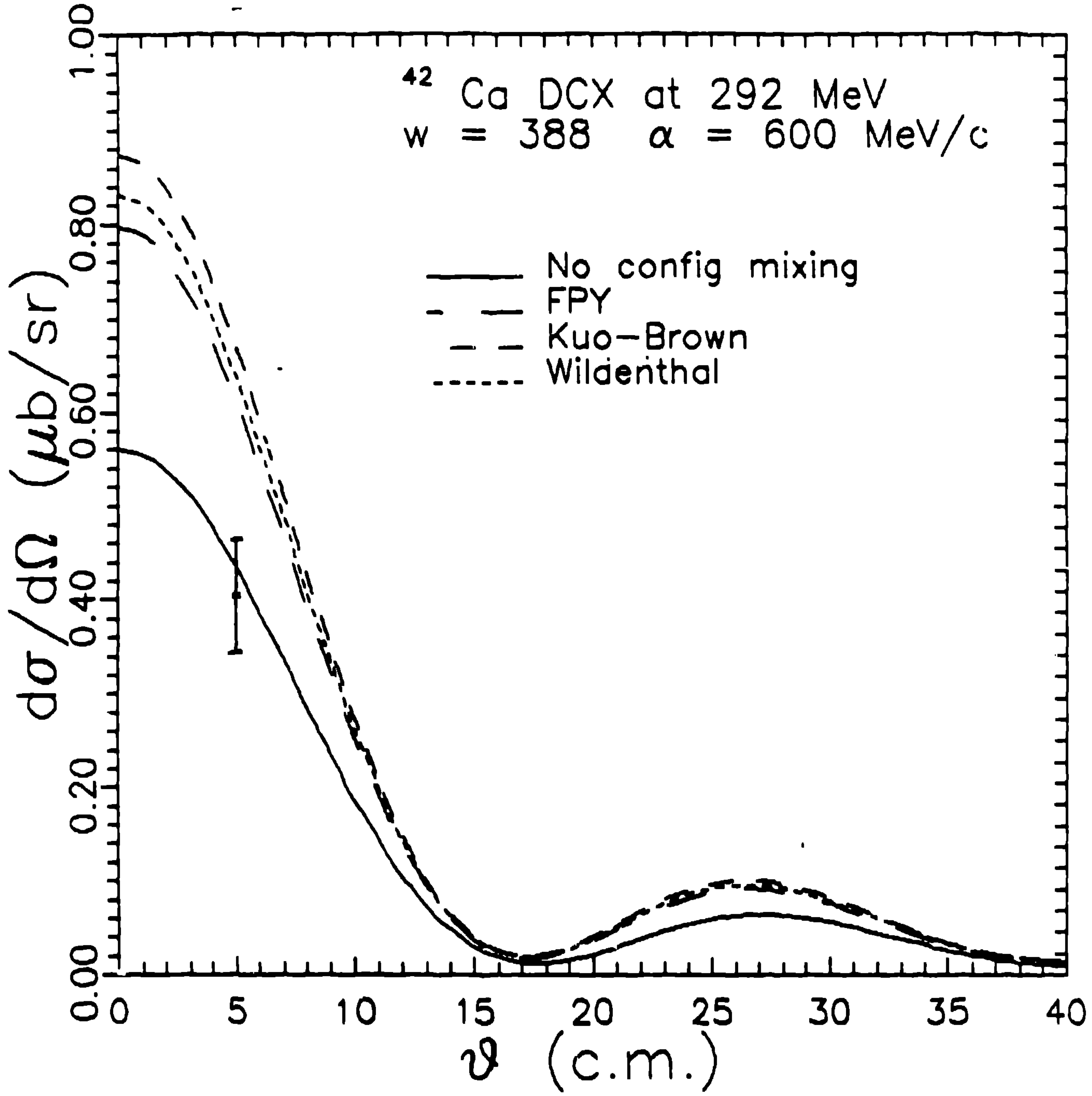

Angular distribution for DCX on ^{42}Ca at 292 MeV. The data is from [18]. Nuclear structure doesn't care about energy so there is a problem, probably the same one seen in comparison of the 292 MeV data for ^{18}O.

Figure 20.